A&A manuscript no.
(will be inserted by hand later)

Your thesaurus codes are:
11(11.01.2; 11.09.1 NGC 6951; 11.11.11; 11.14.1; 11.19.2; 11.19.6)

ASTRONOMY AND ASTROPHYSICS

arXiv:astro-ph/9909495v1 29 Sep 1999

Circumnuclear structure and kinematics in the active galaxy NGC 6951 ⋆ ⋆⋆

Enrique Pérez[1] ⋆⋆⋆, Isabel Márquez[1], Ignacio Marrero[1], Florence Durret[2], Rosa M. González Delgado[1], Josefa Masegosa[1], José Maza[3], and Mariano Moles[4] †

[1] Instituto de Astrofísica de Andalucía (CSIC), Apartado 3004, 18080 Granada, Spain
[2] Institut d'Astrophysique de Paris, CNRS, Université Pierre et Marie Curie, 98bis Bd Arago, 75014 Paris, France
[3] Departamento de Astronomía, Universidad de Chile, Casilla 36-D, Santiago, Chile
[4] Instituto de Matemática y Física Fundamental (CSIC), Madrid, Spain, and Observatorio Astronómico Nacional, Madrid, Spain

Received / Accepted

Abstract. A study is presented of the central structure and kinematics of the galaxy NGC 6951, by means of broad band $B'IJK$ images and high resolution high dispersion longslit spectroscopy, together with archival HST WFPC2 V and NICMOS2 J and H images. We find that there is little ongoing star formation inside the bar dominated region of the galaxy, except for the circumnuclear ring at 5 arcsec radius. There is some evidence that this star formation occurs in two modes, in bursts and continuously, along the ring and inwards, towards the nucleus. The equivalent width of the Ca II triplet absorption lines show that, in the metal rich central region, the continuum is dominated by a population of red supergiants, while red giants dominate outside. The gaseous kinematics along three slit position angles, and the comparison with the stellar kinematics, suggest the existence of a hierarchy of disks within disks, whose dynamics are decoupled at the two inner Linblad resonances (ILR), that we find to be located at 180 pc and at 1100 pc. This is supported by the structure seen in the high resolution HST images. The nucleus is spatially resolved in the emission line ratio [N II]/Hα, and in the FWHM of the emission lines, within a radius of 1.5″, just inside the innermost ILR. Outside the iILR, the stellar CaT velocity profile is resolved into two different components, associated with the bar and the disk. Several results indicate that this is a dynamically old system: the little ongoing star formation inside the bar dominated part of the galaxy, the very large relative amount of molecular to total mass within the inner 6 arcsec radius, $\sim 25\%$, and the geometry of the circumnuclear ring that leads the stellar bar at a position angle greater than 90°. It is thus possible that a nuclear bar has existed in NGC 6951 that drove the gas towards the nucleus, as in the bars within bars scenario, but that this bar has already dissolved by the gas accumulated within the circumnuclear region. We discuss the possibility that the kinematical component inside the iILR could be due to a nuclear outflow produced by the combined effects of SN and SN remnants, or to a nuclear disk, as in the disk within disk scenario that we propose for the fueling of the AGN in NGC 6951.

Key words: galaxies: active – galaxies: individual: NGC 6951 – galaxies: kinematics and dynamics – galaxies: nuclei – galaxies: spiral – galaxies: structure

1. Introduction

The centers of spiral galaxies are frequent sites of activity, marked by the presence of intense star formation (SF) and/or an active galactic nucleus (AGN). This activity needs to be fueled with a supply of gas, whose reservoir can be provided by the disk of spiral galaxies. An efficient way for this gas to lose its angular momentum is provided by the existence of non-axisymmetric components of the galactic potential, together with a strong central gravitational potential. The latter is necessary to explain that AGNs, irrespective of the presence of morphological perturbations, appear preferentially in early type spirals,

Send offprint requests to: Enrique Pérez

⋆ Based on observations made with the 4.2m William Herschel Telescope operated by the Isaac Newton Group, and the 2.6m Nordic Optical Telescope operated jointly by Denmark, Finland, Iceland, Norway, and Sweden, on the island of La Palma in the Spanish Observatorio del Roque de los Muchachos of the Instituto de Astrofísica de Canarias.

⋆⋆ Also based on observations made with the NASA/ESA Hubble Space Telescope, obtained from the data archive at the ESA Space Telescope European Coordinating Facility.

⋆⋆⋆ Visiting astronomer, German-Spanish Astronomical Centre, Calar Alto, operated by the Max-Planck-Institute for Astronomy, Heidelberg, jointly with the Spanish National Comission for Astronomy.

† On sabbatical at Queen Mary and Westfield College, Astronomy Unit, London, UK

Correspondence to: eperez@iaa.es

with the frequency peak at Sb. On the other hand, galaxies dominated by disk star formation occur preferentially in later types with a distribution peaking at Scd (Moles et al. 1995; Ho et al. 1997a and references therein).

The existence of gas to fuel the circumnuclear activity is necessary but not sufficient (e.g., Moles et al. 1995; Maoiolino et al. 1997; Mulchaey & Regan 1997). The right dynamical and physical conditions must exist for this gas to be used effectively in either infalling to the nucleus proper, and feeding the AGN or nuclear starburst, or collapsing by self-gravity in the circumnuclear region in the form of intense SF. There are examples of galaxies where the gas is known to be available in the central regions, but where the onset of SF has yet to occur. For example, NGC 4151, which harbours a Seyfert type 1 nucleus, has a circumnuclear ring of material discovered in the form of dust extinction, and has a large column of neutral hydrogen towards the nucleus, but there is no significant star formation occurring at present (Robinson et al. 1994; Vila-Vilaró et al. 1995; Mundell et al. 1995). However, in the circumnuclear ring of star formation in the target galaxy of this paper, NGC 6951, Kohno et al. (1999) find that although the dynamical shocks provide the mechanism for the accumulation of molecular gas along the ring, this may not be the mechanism responsible for the star formation, but rather the gravitational instability of the clouds thus formed is the driving force for the onset of star formation.

To understand what are the conditions and mechanisms for the onset of nuclear activity in spiral galaxies, a detailed characterisation of morphological and kinematical components in galaxies of different morphology and activity level is needed. The DEGAS collaboration was established to address such a detailed study in a small sample of spirals with an AGN, selected as isolated to avoid the possible external contribution to the assymmetries in the potential. We plan to procede with a parallel analysis of a sample of isolated non-AGN spirals, to look for differences and/or similarities and their implications. IR imaging data of the complete sample are presented and analysed in Márquez et al. (1999a, 1999b). Other recent IR imaging studies of active and control samples include McLeod & Rieke (1995), Mulchaey et al. (1997), and Peletier et al. (1998).

In this paper we present the first results for the SAB(rs)bc galaxy NGC 6951. There are a number of studies of this galaxy that include broad and narrow band optical and infrared images (Buta & Crocker 1993; Márquez & Moles 1993, hereafter MM93; Barth et al. 1995; Wozniak et al. 1995; Elmegreen et al. 1996; Friedli et al. 1996; Rozas et al. 1996a,b; González Delgado et al. 1997; González Delgado & Pérez 1997; Mulchaey et al. 1997), spectroscopy of the nuclear region (e.g., Boer & Schulz 1993; Filippenko & Sargent 1985; Muñoz-Tuñón et al. 1989; MM93; Ho et al. 1995, 1997b; Ho et al. 1997c), radio interferometric maps (Vila et al. 1990; Saikia et al. 1994), and high resolution spectroscopic molecular maps (Kenney et al. 1992; Kohno et al. 1999). To better characterize the detailed kinematical components and their relation to the morphological structures, we have obtained high resolution, high dispersion spectroscopic observations of the gaseous and of the stellar components, and direct imaging in optical and infrared bands.

This paper is structured as follows. In section 2 we present the imaging and spectroscopic data. Sections 3 and 4 detail the results from the analysis of the images and from the spectroscopy respectively, while in section 5 we discuss these results into a common picture of NGC 6951. Section 6 gives the summary and our main conclusions.

2. Observations and data reduction

The journal of observations, given in Table 1, summarizes the spectroscopic and imaging observations carried out with different telescopes and instrumental setups, and those retrieved from the HST archives.

2.1. Spectroscopy

We observed NGC 6951 on the night of 9/10 August 1996 with the ISIS double spectrograph attached to Cassegrain focus of the 4.2m William Herschel Telescope, and the gratings B1200 in the blue arm and R1200, simultaneously, in the red arm. The observations include three wavelength ranges: one range around Hβ and one around Hα (both through the blue arm of ISIS), and a near infrared wavelength range around the Ca II triplet absorption lines through the red arm of ISIS. At each slit position angle we took two 1800 s integrations in the red arm, each simultaneous with one 1800 s in the Hβ and one 1800 s in the Hα ranges.

The gratings provide a linear dispersion of 0.39 Å/pixel, and the wavelength ranges covered with the TEK1 and TEK2 CCD chips used are 4757-5141 Å, 6493-6881 Å in the blue arm, and 8506-8882 Å in the red arm. We used a slit width of 1 arcsec, that projects onto 2.1 pixels (0.81 Å) at the detector. The spatial sampling along the slit is 0.36 arcsec/pixel. NGC 6951 was observed at three slit position angles: the major axis at 138°, the minor axis at 48°, and an intermediate position at 84°.

The observing was performed under photometric atmospheric conditions. At the WHT the seeing is measured continuously with a guide star; it was slightly variable during the observations of NGC 6951, with a median value of 1.2 ± 0.1 arcsec. The phase of the moon was grey.

The reduction of the spectroscopic data followed the standard steps of bias subtraction, flatfield correction, wavelength calibration with a CuNe lamp observed before and after the target, atmospheric extinction correction, and flux calibration using the spectroscopic standards G24-9, LDS749B, BD284211 and BD254644 observed through an 8 arcsec wide slit. Cosmic ray hits were removed individually from the 2D frames. Finally the sky

background was subtracted from each frame using the outermost spatial pixels free from galaxy contribution. The two exposures in the CaT range were added together after checking that the spatial and spectral alignment was good to a small fraction of a pixel. FIGARO and IRAF[1] were used throughout the calibration and analysis phases.

2.2. Optical imaging

Optical images through two continuum filters, B' and I, were taken with the Brocam II camera on the Cassegrain focus of the 2.56m Nordic Optical Telescope during the nights of 8 and 9 October 1996. B' is a special purpose made filter with a square spectral response centered at 4630 Å and with a FWHM=290 Å, so that it does not include any bright emission line. The equivalent width of any emission line within the I filter is negligible. Imaging through emission line free filters is important to ascertain the true circumnuclear stellar structure, that can otherwise be significantly distorted with standard broad band filters, where the emission lines can make an important flux contribution (Vila-Vilaró et al. 1995). The detector was a 1024×1024 Tektronix chip with a sampling of 0.176 arcsec/pixel and a 3×3 arcmin field of view. Weather conditions were photometric and the average FWHM of the seeing profile is 0.8 arcsec. The journal of observations is included in Table 1.

The reduction and calibration of the images has been carried out in IRAF. Bias and flat field corrections were done in a standard way. The task COSMICRAYS was used for the overall cosmic ray removal.

The final image of NGC 6951 for a given filter is obtained by adding all the images for that filter properly aligned, sky subtracted and calibrated. The alignment, using cross-correlation techniques involving only bright stars, is made to an accuracy of 0.1 pixel. The sky background is estimated by averaging the median flux in a few 40×40 pixel patches located outside the galactic disk. The 3σ background limit magnitudes are 20.7 and 21.0 mag arcsec^{-2} in B' and I, respectively.

2.3. Infrared imaging

Infrared images through the filter K' (λ_c=2.10 μ, width=0.34 μ) were taken with the MAGIC camera attached to the Cassegrain focus of the 3.5m telescope at the German-Spanish Observatory in Calar Alto on 1996 September 26. The detector was a Rockwell 256×256 pixel NICMOS3 array, and the camera was set up in the high resolution mode of the f/10 focus, giving a sampling of 0.32 arcsec/pixel and a field of view of 82″×82″. The observation procedure consisted in 3×3 mosaic patterns of the object and nearby sky, alternating the exposures. The mosaic on the galaxy has a 90% overlap between the component tiles. During the observations, the seeing was 1.0 arcsec and the conditions photometric. Each galaxy frame was subtracted from a median sky frame and divided by the flat field. The nine frames were recentered using two or three field point sources and the nucleus, and subsequently they were median averaged. The flux calibration was performed with observations of the Kitt Peak faint standard stars numbers 30, 31 and 32.

NGC 6951 was observed on 1996 September 30, as one of the targets of the BARS collaboration, through the filters J and *Kshort* (*Ks*) with the ARcetry Near-Infrared CAmera, ARNICA, attached to the 2.56m Nordic Optical Telescope in La Palma. ARNICA uses a NICMOS3 array that gives a pixel scale of 0.51 arcsec/pixel and a field of view of 130″×130″. We integrated 40 seconds on the object (dithered in 11 positions) and the same time on the sky, for a total integration time on the object of 440 s in J and 880 s in *Ks* (with a 10″ shift between the different images to facilitate bad pixel removal). Since the size of the galaxy is much larger than the field of view, we repeated the process four times, with the central region of NGC 6951 in common, placed in one of the corners. This allowed us to obtain a final mosaic image with a total integration time of 1760 s in J (3520 s in *Ks*) in the central 2′ and 440 s in J (880 s in *Ks*) in the rest. Flat-field frames were obtained from the median of the sky frames taken along the night. Sky-subtracted and flat-fielded images were then aligned by using a number of foreground stars. We observed 4 standard stars for the flux calibration, leading to a photometric accuracy of 10%. For all the reduction and calibration steps we used the package `sqiid` within IRAF. We measure a FWHM for the stars in the final mosaic of 1.3″. The 3σ limiting magnitudes are 18.8 in J and 19.5 in *Ks*.

2.4. HST images

We have retrieved archival HST images taken with the WFPC2 through the V filter (547M), with a single exposure of 300 s, and with the NICMOS2 camera through the J (110W) and H (160W) filters, with exposures of 128 s each. The spatial sampling of the central PC image in the WFPC2 camera is 0.046″, and 0.075″ for the NIC2 camera of NICMOS. The useful field of view is ∼12″×12″, which contains the circumnuclear region.

3. Imaging results

Fig. 1 shows the B' and Ks images of the galaxy. The most conspicuous features in both images are the bar, the

[1] The authors acknowledge the data analysis software FIGARO provided by the Starlink Project which is run by CCLRC on behalf of PPARC. IRAF is the Image Analysis and Reduction Facility made available to the astronomical community by the National Optical Astronomy Observatories, which are operated by the Association of Universities for Research in Astronomy (AURA), Inc., under contract with the U.S. National Science Foundation.

bulge and the spiral arms. The bar is better traced in *Ks*, since the distortions produced by the dust lanes are minimized. The circumnuclear ring and dust lanes are more clearly traced in B', where they appear as straight features from the bar edges towards the center, curving approximately within the bulge radius. All the ring features reported by Buta & Crocker (1993) are visible: (pseudo) outer, (pseudo) inner and circumnuclear rings, with sizes in agreement with those given by them, and also with optical and/or near-infrared images previously published (MM93, Friedli et al. 1996). We note the isophote twisting in the central parts, from the bar to the circumnuclear ring.

To parametrize the results of the photometric analysis, we have obtained the isophotal profiles by using the task `ellipse` within `stsdas.analysis.isophote` in IRAF, which uses the ellipse fitting method. All the stars in the frame were previously masked. The results are given in Fig. 2, where we plot isophotal magnitudes, ellipticity and position angle (PA) as a function of the square root of the radial distance for B', *I*, *J* and *Ks* bands. They agree with previous results by Friedli et al. (1996), who observed NGC 6951 with a similar configuration, although our data extends 30 arcsec further out. Since the area covered by our optical images is smaller than for MM93, and considering that the faintest isophotes we reach in NIR are still contaminated by the spiral arms, we have decided to use the disk major axis position angle and inclination as determined by MM93, i.e., $\phi = 138^\circ$ and $i = 42^\circ$. These values are compatible with the outermost ellipses as traced by the sharp-divided images, and are in good agreement with the kinematically derived position angle and inclination, as we will see below.

To quantify the bar extension we have computed the amplitude and phase of the Fourier transform applied to the deprojected image, as explained in Márquez & Moles (1996). The mode m=2 has a constant phase out to $45''$, that we adopt as the bar extension.

The isophotal profiles indicate the presence of the circumnuclear ring and bar components, that appear as an excess around $5''$ for the former and from $20''$ to $50''$ for the second. These excesses are clearer once the photometric decomposition is made. We have fitted an exponential disk for the outermost radii, subtracted it from the profile, fitted an $r^{1/4}$ for the resulting bulge, subtracted it from the profile, and iterated until convergence is achieved. The results from the decomposition should be taken with caution since the bar contamination and the dust obscuration are very important. The results for the infrared image are presented in Márquez et al. (1999).

B'-*I* and *J*-*Ks* full size colour images are shown in Fig. 3. In B'-*I* the reddest features trace the dust lanes, most outstanding in the western side of the bar, while the bluest colours trace the regions of active star formation, that occur in the spiral arms outside a 30 arcsec radius. Within the part of the galaxy dominated by the bar structure there is very little ongoing star formation, except in the circumnuclear ring that is delineated by a number of blue knots. A comparison with the Hα image (fig. 5 in MM93; fig. 10 in González Delgado et al. 1997) shows that, for most regions, the Hα flux correlates with the colour B'-*I*, however the bluest large region at 46 arcsec along position angle 20° does not have a correspondingly bright Hα emission, indicating that it may be a star forming region in the post-nebular phase. A detailed analysis of the stellar populations in NGC 6951 will be presented in a future paper. In the two colour maps, bulge and bar colours are very similar.

The highest contrast in the *J*-*Ks* image occurs around the western side of the circumnuclear ring, and along the western dust lane close to the ring. To look at these in more detail, Fig. 4 shows B'-K' and *I*-K' colour maps, where K' is the Calar Alto image, that has better sampling and seeing. Along the dust lanes, the colour contrast is higher in B'-K', that results from a larger dust absorption in B' than in *I*. For the reddest regions inside the circumnuclear ring, the situation is the opposite, with redder colours in *I*-K', in particular, close to the two ends of the ring major axis (NW-W and SE-S), and the SW zone where the ring connects with the bar. This higher contrast in *I*-K' is similar to *J*-*Ks* in Fig. 3. The smaller contrast of the dust in B'-K' can be explained by an excess of B' produced by the ongoing star formation in the ring. Thus the colour maps can be qualitatively understood in terms of the combined effects of dust obscuration and stellar population.

The HST WFPC2 *V* image has been published and analysed by Barth et al. (1995), that study the distribution of super star clusters in the circumnuclear ring. The HST NICMOS images have not been published yet. In Fig. 5 we show the *J*-*H* colour image. The red features contouring the circumnuclear ring are visible in great detail, mainly delineated as two short spiral arms that trace the ends of the oval. Closer to the nucleus, it consists of a number of small knots and structures that delineate a multi-spiral like structure.

4. Spectroscopic results

4.1. The emission line spectrum

The three slit orientations used are depicted in Fig. 6, that shows the Hα contours (from the data of González Delgado et al. 1997) on a B′/K′ grayscale colour map. The three position angles correspond to the major axis (PA=138°), the minor axis (PA=48°), and an intermediate angle (PA=84°). The slits cross the circumnuclear ring, but only one of the bright Hα knots.

We have measured the emission line intensities at every spatial increment along the slit, by means of fitting gaussian components with LONGSLIT (Wilkins & Axon 1991). Fig. 7 shows the spatial variations of the Hα line

intensity and the Hα/Hβ ratio for position angles (a) 48°, (b) 84° and (c) the major axis at 138°. The Balmer lines are affected by underlying absorption components in the nucleus and in the ring H II regions. A detailed analysis of the stellar population contributing to the Balmer absorption is beyond the scope of this paper, but a comparison of the spectra with evolutionary population synthesis profiles of the Balmer absorption line profiles (González Delgado et al. 1999b), indicates that the Balmer emission lines should be corrected by a line core equivalent width of 1 Å in the nucleus and 0.5 Å in the ring; this result is found through the comparison of the absorption wings detected in the Hα and Hβ lines and in the nearby metal absorptions with the predictions of the models. The Hα/Hβ ratio shown in Fig. 7 has been corrected in this manner. The Balmer emission line ratio maps the effect of extinction by the dust lanes; it is high in the nucleus (Hα/H$\beta \geq 10$ at the center), then becomes smaller in the transition region between the nucleus and the ring of H II regions (Hα/H$\beta \simeq 4$ at a distance of ±1.5 arcsec), and increases again across the ring to reach values of Hα/H$\beta \simeq 10$ in the outer side of the ring. This reddening across the ring is clearly produced by the dust lanes, as seen in Fig. 4. The extinction that corresponds to the above values of the Balmer ratio is c(Hβ)=1.6, 0.4, and 1.6 mag for the nucleus, the transition region and the ring respectively. Thus, just outside the partially resolved nucleus, at ±1.5 arcsec, the extinction reaches a minimum and the Balmer ratio takes the case B value. The HST image in Fig. 5 shows indeed little dust in that intermediate region. The Galactic extinction towards NGC 6951 quoted in the NED IPAC database is 0.88 mag in B, corresponding to E(B-V)=0.22 or c(Hβ)=0.31, i.e. most of the extinction that we measure in the intermediate region between the nucleus and the circumnuclear ring is of Galactic origin and not intrinsic to NGC 6951.

Fig. 8 shows the line ratio [N II]6583/Hα together with the Hα and [N II] fluxes. For all three PA the ratio becomes larger than unity within the inner ±2 arcsec, reaching values of 5 in the nucleus. This large ratio is due to a strong increase in the [N II] flux and not to underlying absorption in Hα. Indeed, the [N II] takes normal H II region values in the ring, but increases sharply inwards. This region of high [N II]6583/Hα is significantly more extended than the nuclear point spread function, and thus it is spatially resolved. The [S II]/Hα ratio (not shown) also shows a qualitatively similar behaviour, with an increase from [S II]/Hα=0.18 in the ring H II regions to [S II]/H$\alpha \geq 1.8$ in the nucleus. The electron density, computed from the line ratio [S II]6717/6731, increases from low values, $N_e \sim 300$ cm^{-3}, in the ring H II regions to values larger than 1000 cm^{-3} within the inner region and the nucleus (cf. Table 2). These [N II] and [S II] line ratios seem to indicate the presence of a shocked component, also supported by kinematical evidence, as explained below.

Fig. 9 shows the Hβ and [O III] 5007 line fluxes along PA 138°. The nucleus has a high excitation. The [O III] flux decreases sharply to reach a ratio [O III]5007/H$\beta < 1$ outside ±2 arcsec from the nucleus. Thus the ring H II regions have very low excitation; in fact, we cannot measure [O III] 5007 pixel by pixel outside the nuclear component at any of the three position angles. In order to compute this excitation ratio for the ring H II regions, we have extracted three one-dimensional spectra at each position angle, integrating the nucleus and the two sides where the slit crosses the ring. Fig. 10 shows these for PA=48°. The measured Hβ and [O III] 5007 line fluxes and the ratio [O III]5007/Hβ are given in Table 3, as well as the ratio with the Hβ flux corrected for underlying absorption (an absorption equivalent width of 1 Å in the nucleus and 0.5 Å in the H II regions).

4.2. The absorption calcium triplet spectrum

We have measured the equivalent width of the two main CaT lines at $\lambda\lambda 8542, 8662$Å, according to the method described by Díaz, Terlevich & Terlevich (1989, hereafter DTT). The nuclear spectrum (central 0.72 arcsec) is plotted in Fig. 11 for reference; the three CaT lines, MgI λ8807, and two of the hydrogen Paschen lines in absorption are identified. The weakness of Pa14 indicates a negligible contamination of the CaT lines by Pa16, Pa15 and Pa13, that fall in their red wings. The results of the pixel to pixel equivalent width measurements along the slit, for the three position angles, have been combined and are shown in a single Fig. 12. The lefthand side of this figure, (-10 arcsec to the nucleus) corresponds to the NE–SE quadrant on the eastern side of the galaxy. The righthand side of the figure (from the nucleus to 10 arcsec) corresponds to the NW–SW quadrant on the western side. There is a clear systematic trend in this combined figure, that can also be appreciated (albeit with a worse signal-to-noise ratio) along the three individual PA. Outside the circumnuclear ring, ew(CaT) takes a low value of ~ 5.5 Å; at and within the ring, 5 arcsec east and 4 arcsec west, ew(CaT) jumps to a higher value of 7 Å; and closer in, within the partially resolved nucleus, ew(CaT) rises to a value between 8 and 9 Å. These are three distinct regimes clearly present in the circumnuclear region.

The interpretation of ew(CaT) as a function of a stellar population depends on the metallicity (DTT; see the most recent work by García-Vargas, Mollá & Bressan, 1998, and references therein). We can have an indication of the metallicity by measuring the ew(MgI). According to DTT this line is sensitive to metallicity and to effective temperature, but not to gravity. In the nucleus of NGC 6951, ew(MgI)$\geq$ 0.8 Å, that indicates (see fig. 8 of DTT) the production by cool ($T_{\rm eff} < 4700$ K), high metallicity stars (solar or higher). For this metallicity range, ew(CaT) is a function mainly of gravity and so we can now interpret the measurements in terms of stellar populations.

The lowest values of ew(CaT), present mainly outside the ring, are due to an old stellar population of giants, with an age around 0.5 to 1 Gyr. The highest nuclear values, ew(CaT)$\geq$ 8 Å indicate the presence of an important population of red supergiant stars (RSG), that dominate the luminosity at these wavelengths, with an age around 10 to 20 Myr. In the circumnuclear region, ew(CaT) takes intermediate values; it is significantly higher than in the outer parts, but the actual value belongs to a range that can be explained by either giants or RSG. Our interpretation is as follows. The measured equivalent widths in the circumnuclear and nuclear regions are a lower limit to the actual values, for two reasons. First, these equivalent widths are diluted by the continuum of the young stellar population responsible for the ionization of the gas; we cannot precisely gauge with our present data set how important is this dilution, for which we would need spectroscopy in a longer wavelength range, including the ultraviolet, but we do see the blue stellar knots so that some dilution by them must be taking effect. Second, at least outside a radius of 2 arcsec, we can distinguish two distinct stellar kinematical components; although we cannot measure independently their contribution to the luminosity or to the ew(CaT), it is at least possible that one of these two distinct populations (one that can be identified with the bar population) contributes to dilute the other population (whose kinematics is dominated by rotation, see below). Thus, if dilution is taken into account it is likely that the circumnuclear values of ew(CaT)$\sim$ 7 Å are in fact larger, so that they also reflect a population of RSG within the ring.

4.3. Gas kinematics

We have measured the systemic velocity in Hα by integrating all the spatial increments along the slit corresponding to the disk emission (i.e. excluding the nucleus and the circumnuclear ring of H II regions), and fitting the two peaks of the resulting integrated profile. The mean velocity of these two peaks is 1417$\pm$4 km s^{-1}; this corresponds to a scale of 92 pc/arcsec, for H$_0$=75 km s^{-1} Mpc^{-1}. The velocity curves obtained from the pixel to pixel measurements of the Hα emission line are shown in Fig. 13; the Hα line flux is also plotted for reference. Allowing for the different spatial and spectral resolutions, these velocity curves agree very well with those presented by MM93. In the following we analyze the detailed and the global kinematic structures found along the three position angles.

First we confirm that PA=138° presents the largest velocity amplitude, followed by PA=84° and PA=48°, indicating that 138° is closest to the major axis. At first glance, there seems to be much velocity structure at PA=48° that does not correspond to a kinematic minor axis, where we would not expect a systematic residual velocity curve. On a more detailed analysis, this velocity structure present along PA=48° is related to local morphological structure, and we can see that the outer parts of the disk velocity correspond to the systemic velocity, as indicated by a horizontal dotted line, 1417 km s^{-1}. Thus we adopt 48° and 138° as the kinematic minor and major axes respectively.

For this value of the kinematic major axis and an inclination angle of 42° (MM93), the total dynamical mass enclosed within the circumnuclear region (a radius of 6 arcsec, equivalent to 644 pc), is $M = r\,v^2/G = 5.8 \times 10^9$ M$_\odot$. Kohno et al. (1999) report a *molecular* gas mass of 1.4×10^9 M$_\odot$ within a 6 arcsec radius; this amounts to 25% of the total dynamical mass.

Much detailed structure is present in the velocity curves at the different PA. For example, at PA=48° we detect the 50 km s^{-1} streaming into the main NE arm, between -56.5 arcsec and -53 arcsec (labelled A in Fig. 13). Also at this PA we detect the 50 km s^{-1} streaming into the bar region at -36 to -20 arcsec in the NE (labelled B), and at 32 to 23 arcsec to the SW (labelled B$'$). At PA=84°, the 50 km s^{-1} streaming into the bar is seen at the eastern edge, between 40 and 30 arcsec (labelled C), and at the western edge of the bar between 39 and 32 arcsec (labelled C$'$).

When deprojected for an inclination of 42° and a kinematic major axis of 138°, the velocity curves at PA 84° and at PA 138° generally match in the outer disk regions, except for local distorsions produced by the spiral arms. However, the circumnuclear region shows a different picture. One important feature of the velocity curve at PA 48° is the existence of an *apparent* counter-rotation of the gas within the circumnuclear region with respect to the gas in the disk at the same PA. Indeed, when we look into the $\pm$8 arcsec circumnuclear velocity gradients at the three position angles more closely (insets in Fig. 13), we see three features. First, if we deproject the circumnuclear velocity curves using the same two parameters as for the main disk, $i = 42°$ and $\phi = 138°$, the deprojected amplitude at PA=84° becomes significantly larger than at PA=138°; this would imply that the circumnuclear region requires a different set of deprojection angles. Second, there is a continuous change of slope between the three PA, flattening from PA=138° to PA=84° to PA=48°. If the circumnuclear velocity curve along PA=48° is also produced by disk rotation, then the kinematic axis of this circumnuclear rotation must be different from the kinematic axis of the main disk. Under this assumption of disk rotation, we can compute a kinematic major axis for this circumnuclear region. We obtain that in this case the major axis of the circumnuclear region would correspond to 118°; with this circumnuclear major axis and for the same[2] inclination of 42°, the three deprojected circumnuclear velocity

[2] If this circumnuclear region is a decoupled gaseous disk, it could have a different inclination to the line of sight that the main galaxy disk, but we will assume here that this is not the case and that the inclination is the same.

curves agree quite well. Third, at PA=84°, the circumnuclear velocity amplitude, 200 km s^{-1}, is significantly larger than the galaxy main disk velocity amplitude at the same PA, 130 km s^{-1}. These three facts, namely, the *apparent* nuclear counter-rotation at PA=48° and the greater velocity amplitude at PA=84° (both, with respect to the disk amplitude at PA=84°, and with respect to the deprojected circumnuclear amplitud at PA=138°), argue for a gas dynamics in the circumnuclear region of NGC 6951 that is decoupled from the dynamics of the main body of the galaxy. We shall return to this point in the discussion section.

The FWHM of Hα and [N II] are plotted in Fig. 14. The values shown have been corrected for an instrumental resolution of 43.5 km s^{-1}. The influence of the nuclear velocity gradient on the widths is negligible; the gradient is 44 km s^{-1} arcsec^{-1}, that amounts to a quadratic correction on the nuclear widths of only 2 km s^{-1}. The Hα line flux is shown (dotted) for reference. The velocity dispersion in the circumnuclear region is very high, in the Hα line there is a central plateau of 180 km s^{-1} in the nuclear ±1.2 arcsec, it then decreases down to a minimum of 70 km s^{-1} that is reached at the maximum of Hα emission in the H II regions. After this local minimum, the velocity dispersion increases again to 120 km s^{-1} and above in the two quadrants NE-NW and SE-SW across the ring of H II regions. This trend is consistent with the general picture of the dynamics deduced from our data and from the molecular content (Kohno et al. 1999), that will be developed in the discussion section. The behaviour of the velocity dispersion for the [N II] λ6583 line is qualitatively similar to but systematically higher than that of Hα by a factor 1.2 in the inner ±3 arcsec, reaching values of up to 220 km s^{-1} in the nucleus. These emission line widths indicate dynamically hot nuclear and circumnuclear regions. The kinematic data and the results from the emission line ratios and density values presented in section 4.1 seem to imply the existence of shocked material.

The width of Hα is not resolved further out in the disk of the galaxy, except across the spiral arms where it reaches values of 25 to 45 km s^{-1}.

4.4. Stellar kinematics

We have measured the velocity curve from the two main lines of the Ca II absorption triplet at $\lambda\lambda$8542, 8662 Å, by means of cross-correlating the galaxy frames with seven spectra of five different K giant stars, observed during the same night and with the same setup. These stars are HD132737, HD171232, HD208817, HD198858, and HD1918. The cross-correlation is performed with a 2D procedure we have implemented that makes use of the IRAF function CROSSCORR. The position and amplitude of the peak of the cross-correlation function is measured, and the resulting velocity curves are weight averaged at each position angle. The signal-to-noise ratio of the data allows measurements only within a 20 arcsec radius at PA=84° and 48°, and 10 arcsec at PA=138°. The resulting curves are shown in Fig. 15 (expanded for the central region in the insets) for the three position angles, together with the corresponding Hα emission velocity curves for comparison.

First, we inspect the stellar velocity curves. Inwards of the circumnuclear ring, in the ±2 arcsec radius resolved nuclear zone, there seems to be a normal stellar rotation curve, with a measured gradient of 41 and 26 km s^{-1} arcsec^{-1} at PA=138° and 84°, and flat at PA=48°. Outside this radius it is possible to partially resolve the absorption line profile into two components, that are seen in the cross-correlation function by corresponding local peaks; in most spatial increments one component fully dominates the profile, while in some increments the position of the two components can be more easily measured. The velocities corresponding to these two components are plotted with filled and open symbols in the figure. On either side of the nucleus, these two stellar components have their velocity of the same sign, although their amplitude difference reaches 50 km s^{-1}.

We now look into the comparison with the gas Hα velocity curves. Where only one stellar component is measured, i.e. within the nuclear 2 arcsec radius, the velocity curves of the gas and of the stars at PA=84° and 138° follow each other approximately. This is not the case at PA=48°, where the stellar velocity curve is flat, while the Hα curve presents a slope (c.f. previous section 4.3) with a peculiar structure in the central ±1.5 arcsec.

At PA=84° the nuclear ±1.5 arcsec part of the gaseous and stellar velocity curves both follow the same similar pattern; however, when the two stellar components can be kinematically resolved, neither of them two match the gas kinematics. One component is very flat with a mean velocity of 1440 km s^{-1} from 4.5 arcsec eastwards of the nucleus, and a velocity of 1400 km s^{-1} from 5 arcsec westwards of the nucleus. This stellar component matches the velocity of the gas entrained in the bar both at 30 arcsec east (at 1440 km s^{-1}) and at 30 arcsec west (at 1400 km s^{-1}; c.f. previous section 4.2 and Fig. 15). We shall refer to this component as the *stellar bar component*. The other stellar component is steeper but not as much as the gas component between ±3 arcsec and ±7 arcsec, where the gas presents a significantly larger rotation amplitude than the stellar disk rotation at the same projected distance (a similar case to that reported for the barred galaxy NGC 6701 by Márquez et al. 1996, cf. their fig. 12). The extrapolation of this stellar component meets the gas rotation in the disk at 40 arcsec east (at 1490 km s^{-1}) and at 40 arcsec west (at 1330 km s^{-1}); we shall refer to this component as the *stellar disk component*.

At PA=138° the stellar velocity presents a similar behaviour. Only one component is apparent within a 3 arcsec radius; this generally follows the gas velocity, although with less structure in the nucleus. Outwards of this radius two stellar velocity components can be distinguished. At

the south-east the steeper of the two components reaches a maximum velocity of 1553 km s^{-1}, that extrapolates to match the disk gas velocity.

The stars and the gas kinematics are most different at PA=48°. The gas presents an *apparent* counter-rotating component within a 6 arcsec radius with respect to its outer disk rotation, and an additional peculiar velocity structure in the nuclear ±1.5 arcsec. The stars show a slowly rising kinematics from north-east to south-west, compatible with the disk rotation, and there is no indication of any peculiar velocity structure in the nucleus similar to the gaseous one. This peculiar structure in the gas velocity along the minor axis could be due to an off-centered slit, to a gaseous nuclear outflow, or to a structure related to the iILR.

5. Discussion

We shall now discuss the results obtained in the previous sections and try to put them into a coherent picture of the morphology and kinematics of the circumnuclear region in NGC 6951.

5.1. The level of activity in the nucleus: Seyfert 2 or LINER?

The active nucleus in NGC 6951 has been classified in the literature as a Seyfert 2 (e.g., Boer & Schulz 1993; Ho et al. 1995, 1997b) or as a LINER (Filippenko & Sargent 1985; Muñoz-Tuñón et al. 1989; MM93). Of the different classifications, that of Ho et al. (1997b) is the most accurately performed, because of the data quality and the correction for underlying absorption, that affects somewhat to Hα, and more to Hβ. The classification is based on the three Veilleux & Osterbrock (1987) diagrams [O III]5007/Hβ vs. [N II]6583/Hα, [O III]5007/Hβ vs. [S II]6716+6731/Hα, and [O III]5007/Hβ vs. [O I]6300/Hα.

We have extracted the central 1.0 × 1.2 arcsec as the most representative spectrum of the nucleus, and we measure [O III]5007/Hβ=2.59 (5.89), [N II]6583/Hα=7.00 (3.72), and [S II]6716+6731/Hα=3.06 (1.63). For the values in parentheses, Hβ and Hα have been corrected for an underlying 1 Å of equivalent width in absorption (as discussed in section 4.1 above); these are the values used in the diagrams. Further, recently we have had access to a lower resolution spectrum, from where we can measure [O I]6300/Hα ≥0.35. Using these values in the diagrams, the nucleus of NGC 6951 is located in the very high excitation end of the region of these diagrams filled by the LINER points. This explains the uncertain classification, even when the correction for underlying absorption is taken into account. In fact, because the most critical value is [O III]5007/Hβ which is most sensitive to this absorption correction, it makes the precise definite classification somewhat arbitrary. Ho et al. (1997b) classification criteria (cf. their table 5) consider a horizontal boundary between Seyfert 2 and LINERs at [O III]5007/Hβ ≥3; this puts NGC 6951 in their Seyfert 2 zone. Other authors consider that the boundary between the two classes changes with the value of the abscissa (e.g. Gonçalves et al. 1999), and this would put NGC 6951 in the higher excitation end of the LINER zone. In either case, the value of [N II]6583/Hα=3.72 is also very high, that may suggest an overabundance of nitrogen; this will be discussed in a future work on the stellar populations and gas phase abundances.

In summary, the active nucleus in NGC6951 can be considered as a transition object between a very high excitation LINER and a possible nitrogen overabundant Seyfert 2.

5.2. Colour maps: dust and stellar populations

According to numerical simulations and to observations of barred galaxies, the interaction of the bar and the disk creates mildly shocked zones that enhance the formation of H II regions, mainly at the ends and along the leading edges of the bar. This also produces a net flow of disk gas and dust towards the central regions of the galaxy, where the interaction with the bulge and nuclear dynamics often enhances the circumnuclear star formation later in the evolution of these systems. In Fig. 3, the scarcity of star forming regions in the bar (both, at the ends and along the leading front of the bar), and the presence of the circumnuclear ring of star formation, argues for a relatively old dynamical age of the bar and associated systems in NGC 6951. Other imaging and spectroscopic results give further support to this scenario.

When we consider all the information available (cf. sections 3 and 4), a pattern seems to emerge in the circumnuclear region in which:
(a) There is a widespread population of supergiant stars that dominate the light along and inwards of the circumnuclear ring, between about 6 arcsec and 1.5 arcsec radius. These are most clearly seen in the K dominated J-K map, together with the large CaT equivalent widths measured in this same zone (cf. section 4.2).
(b) The correspondence between the regions more luminous in B' and in Hα is only good for the two brightest ones, but there are two regions bright in Hα with apparently no corresponding enhanced B' that must be understood in terms of extinction; and there is widespread enhanced B$'$ along and inwards of the ring with little or no corresponding Hα emission, that indicates star formation in the post-nebular phase. It is interesting to notice that B' is enhanced both locally in a knotty structure along the ring and more diffuse along and inwards of the ring; this might be interpreted as a signature of two modes of star formation coexisting here: continuous and bursting. It is possible that a continuous star formation process with ocasional bursts takes place in a region such as this one, where a more or less steady supply of gas has been going

on for a long time, as supported by the large fraction of molecular to total mass within the region (cf. section 4.3 above).
(c) There is some indication of a time sequence in the star formation history along the ring, more apparent in the W-N quadrant. First, the strong K knot at position angle $\sim$250°. Second, two knots bright both in B' and K with very little diffuse Hα emission at PA=270° and 300°; this is where Kohno et al. (1999) find the leading secondary maximum of HCN distribution, and also the location of the leading secondary maximum of the 6 cm radio emission (Saikia et al. 1994). Third, the H II region to the north, PA=342°, that is brightest in B', Hα, HCN and 6 cm. Finally, the region just behind this one along the ring, partly associated with the CO peak from Kohno et al., and that might be predicted to be the next in the sequence of star formation. A similar, albeit somewhat less well defined, trend is observed in the south-eastern side.

In conclusion, a qualitative look at the colours suggests that there may be two coexisting modes of star formation, continuous and bursting, and that the bursting mode may be sequential from the spearhead backwards along the entrained material as it is shocked in the circumnuclear ring.

Some of the ideas proposed here are only suggested by the wealth of information indicated by the data, and a detailed quantitative analysis of the stellar populations will be necessary to elucidate the validity of some of them. We are gathering spectroscopic data at other wavelengths to address this future analysis.

5.3. Linear analysis of the kinematics

By performing a standard linear analysis of the kinematics (e.g. Binney & Tremaine 1987) it is possible to obtain the location of the main resonances, co-rotation (CR) and the inner Linblad resonances (ILRs). We use results from numerical simulations that place CR close to the bar semi-major axis (Athanassoula 1992), to infer a bar pattern speed of 3 km s^{-1} arcsec^{-1} (32 km s^{-1} kpc^{-1}) [3]. This implies the existence of two ILRs, at 2 arcsec (180 pc, inner ILR) and at 12 arcsec (1100 pc, outer ILR) [4]. From OVRO CO observations of the central part of the galaxy, Kenney et al. (1992) obtain values of 180 pc for the iILR and 460 pc for the oILR; this latter value is a lower limit derived from their upper limit to the bar pattern speed of 66 km s^{-1} kpc^{-1}, and thus is compatible with our results.

5.4. Structure of the circumnuclear region

The linear analysis of the kinematics indicates the existence of a possible iILR at 2 arcsec. Do we see a correlation between this dynamical feature and any morphological or spectroscopic properties?

Morphologically, the Hα, colour, and HST optical images all show structure within the inner 2 arcsec; i.e., it is not a point like nucleus. Friedli et al. (1996) have looked without success for the existence of a secondary bar, that could be possibly associated with the existence of the iILR. There is no indication of such an inner bar either in our images. In fact, the HST optical image shows a clear inward spiraling structure down to 0.5 arcsec radius (46 pc).

Spectroscopically, several diagnostics are spatially resolved within the inner 2 arcsec radius, such as the [N II]/Hα ratio (Fig. 8), the FWHM of both Hα and [N II] (Fig. 14), and the equivalent with of the CaT lines indicating the presence of an important population of red supergiants in the nucleus (Fig. 12). The gaseous and stellar velocity curves also show features within the iILR: for the three PA, the two stellar components merge at the iILR and are no longer distinguishable; the gas velocity curves at PA=84° and 138° flatten within a 1.5 arcsec radius, while at PA=48° the gas velocity shows a peculiar structure within a 2 arcsec radius, that is not present in the stellar velocity.

This peculiar structure along the minor axis could be due to an off-centered slit, to a gaseous nuclear outflow, or to a structure related to the iILR. The first possibility is ruled out because this velocity structure is present only in the ionized gas but not in the stars, that implies that it is a physically existing feature, given that the two spectral regions were observed simultaneously and through the same slit. Of the two other possibilities, our data do not have sufficient spatial resolution to make a more definitive conclusion. However, we can make a few comments. A nuclear outflow could be produced by the combined effect of the winds and supernova explosions of the recent past generation of star formation indicated by the red supergiant stars we have detected. Saikia et al. (1994) give a total flux for the nuclear beam component of NGC 6951 at 6 cm of 1.1 mJy; they argue that this non-thermal flux is most likely due to supernovae. This flux implies a luminosity of 0.47×10^{20} watt Hz^{-1}, that can be converted to a supernova rate using the models of Colina & Pérez-Olea (1992), to give 0.002 yr^{-1}. A similar calculation with the 20 cm radio flux in the nuclear component given by Vila et al. (1990), that implies a luminosity of 1.03×10^{20} watt Hz^{-1}, yields the same value for the SN rate. This is a low SN rate when compared with bright nuclear starbursts such as

[3] Computing the intersection between the bar pattern speed and the curve $\omega - \kappa/2$ (were $\omega(r)$ is the angular velocity and $\kappa(r)$ the epicyclic frequency) directly from the data points in the velocity curve is hampered by the dependence of $\kappa(r)$ on the derivative of the velocity, which implies that small errors and structure in the velocity as a function of radius translate into large fluctuations in $\kappa(r)$. In the case of NGC 6951 this problem is further exacerbated by the scarcity of data points in the region outside the circumnuclear ring, between 10 arcsec and 30 arcsec.

[4] The shallow radial dependence of $\omega(r)$ at this distance from the nucleus, and the steeper dependence closer to the nucleus, implies that a 10% or 20% uncertainty in the position of CR does not affect significantly the location of the ILRs.

NGC 7714, for which González Delgado et al. (1999a) find $0.07\,\mathrm{yr}^{-1}$, but is qualitatively consistent with the faintness of the nucleus in Hα. If a nuclear outflow were the explanation for the kinematic features in the nucleus, we would only be seeing the approaching, blueshifted, side of the outflow with a speed of $\sim$100 km s^{-1}; the typical expansion velocity of a superwind bubble blown by a nuclear starburst in dwarf galaxies is of the order of 50 km s^{-1} (Marlowe et al. 1995); but is significantly larger, a few 100 km s^{-1}, for nuclear superwinds in Starburst galaxies (González Delgado et al. 1998). The receding side would be presumably occulted by a combination of nuclear obscuration and spatial and spectral resolution.

A third possibility suggested by the data is that the nuclear gas dynamics inside the iILR is partially decoupled from that of the circumnuclear region which, in turn, is partially decoupled from that at larger scales. This would be a scenario of nested disks within disks, where a circumnuclear disk accumulates mass from the outer main galaxy disk via the torques produced by the bar, and becomes sufficiently massive to decouple from the main disk dynamics at the oILR; part of this infall proceeds further into the nucleus, where a similar rotating structure (a torus or a nuclear disk such as those seen in HST images, Ferrarese & Ford 1999; Ford et al. 1998) decouples from the circumnuclear disk at the iILR. We notice that the orientation of the ring in NGC 6951 is leading with respect to the inflow of material from the bar, i.e. it is advanced from the perpendicular to the bar, and this relative orientation is seen in numerical simulations only when the system is relatively old (see, for example, figure 3 of Byrd et al. 1994). In this context, it would be possible to interpret the change of the velocity curve in the three PA, within the inner 2 arcsec radius, as produced by rotation in a disk with a minor axis different from the 48° of the main disk, and different from the 30° of the circumnuclear disk (cf. section 4.3); it would have a value somewhere between 84° and 48°, so that at PA=48° we could observe the change of velocity slope with respect to that at 84°.

The appearance of the HST images would support this scenario. Figure 16 shows the HST V and H sharp divided[5] images; the H image shows a very uniform stellar light distribution in the transition zone between the ring and the nucleus. However, the V image shows a structure spiralling inwards, delineated by the dust that can be traced right into the nuclear 0.5 arcsec. Thus, these high resolution images show both the lack of any inner bar-like structure and the existing of a continuing spiralling into the nucleus, similar to that found in numerical simulations by Piner et al. (1995, cf. their fig. 4). A similar conclusion has been recently reached by Regan & Mulchaey (1999), who have looked for evidences of strong nuclear bars in WFPC2 and NICMOS2 images of a sample of Seyfert galaxies, and find evidence of the existence of this nuclear bar in only 3 out of 12 galaxies studied, while the majority of the galaxies show a spiral morphology similar to what we find in NGC 6951. This does not necessarily implies that the 'bars within bars' mechanism proposed to fuel the nucleus has not been at work in these galaxies (Shlosman et al. 1989; Friedli & Martinet 1993); at least in NGC 6951 we have found several indications that point to a system that is dynamically old, in particular, the large percentage of molecular mass accumulated in the nucleus, $\sim 25\%$, could have already occasioned the dissolution of a nuclear bar, and be working towards the desassembling of the large scale bar.

This idea is inferred from extrapolations of three slit PA. While we understand that a complete 2D spectroscopic mapping of this and other galaxies is required to confirm or otherwise dismiss it, it is also true that such a 2D mapping at a spectral *and* spatial resolution equal to or better than our data is very difficult to obtain with present day instrumentation. Recent developments like SAURON (Miller et al. 1999) and similar instruments will have an important impact on such studies in the next few years.

[5] This process of enhancement consists in dividing the original image by a median filtered version, so as to enhance sharp features.

6. Summary and conclusions

We have obtained broad band $B'IJK_s$ images and high resolution high dispersion longslit spectroscopy for the ionized gas (around Hβ to [O III] and Hα to [S II]), and for the stellar populations (in the Ca II triplet lines around 8500 Å) of the galaxy NGC 6951. Together with archival HST VJH images, we analyse these data to study the central structure and kinematics and find that:

- There is little star formation ongoing inside the bar dominated region of the galaxy, except for the circumnuclear ring at 5 arcsec radius. There is some evidence that this star formation occurs in two modes, in bursts and continuously, along the ring and inwards towards the nucleus.
- The nuclear spectrum shows both very high excitation and very strong [N II] and [S II] lines, making the classification of the AGN somewhat uncertain between a high excitation LINER and a possibly high nitrogen abundant Seyfert 2, depending mainly on the uncertain correction for underlying absorption in Hβ. The electron density varies between 300 cm^{-3} and 1000 cm^{-3}.
- The equivalent width of the Ca II triplet absorption lines show that in the metal rich central region of this galaxy, within 5″ radius, the continuum light is dominated by a population of red supergiant stars, while outside the circumnuclear ring the stellar population is that of giants.
- We suggest that the gaseous and stellar kinematics along the three slit position angles can be interpreted as the existence of a hierachy of disks within disks, with

dynamics decoupled at the two ILRs, that we find to be located at 180 pc and at 1100 pc. This would be supported by the structure seen in the high resolution HST images.
– The nucleus is partly resolved within a radius of 1.5″ (just inside the iILR) both in the emission line ratio [N II]/Hα, and in the FWHM of the emission lines.
– Outside the iILR the stellar CaT velocity profile can be partly resolved into two different components that seem to be associated to the bar and to a disk.
– We discuss the possibility that the kinematic component inside the iILR could be due to a nuclear disk, as in the disk within disk scenario suggested above, or to a nuclear outflow produced by the combined effects of SN and SN remnants.
– Several clues indicate that this is a dynamically old system: (i) there is little star formation ongoing inside the bar dominated part of the galaxy (except for the circumnuclear ring), (ii) the relative amount of molecular to total mass within the inner 6 arcsec radius is very large $\sim 25\%$, and (iii) the geometry of the circumnuclear ring leading at a position angle greater than 90° from the stellar bar. It is thus possible that a nuclear bar has existed in NGC 6951 that drove the gas towards the nucleus, as in the bars within bars scenario, but that this bar has already dissolved by the gas accumulated within the circumnuclear region.

Acknowledgements. Thanks to Hector Aceves for precise comments and clarifications, and to Jaime Perea for SIPL. This work is financed by DGICyT grants PB93-0139 and PR95-329. We acknowledge financial support from INSU-CNRS for several observing trips and from the Picasso program of the French Ministry of Foreign Affairs for several collaboration trips. EP thanks the Director of the Space Telescope Science Institute for the occasion to visit the Institute during the course of this research. The Space Telescope Science Institute is operated by AURA, Inc., under NASA contract NAS5-26555. We are very grateful to Ron Probst, who made available to us the SQIID package for the reduction of infrared images within IRAF. The BARS project has received observing time under the International Time Programme offered by the CCI of the Canary Observatories, and financial support by the European Commission through the Access to Large-Scale Facilities Activity of the Human Capital and Mobility Programme. This research has made use of the NASA/IPAC extragalactic database (NED), which is operated by the Jet Propulsion Laboratory, Caltech under contract with the National Aeronautics and Space Administration.

References

Athanassoula, E., 1992, MNRAS 259, 345
Barth, A.J., Ho, L.C., Filippenko, A.V., Sargent, W.L., 1995, AJ 110, 1009
Binney, J., Tremaine, S., 1987, Galactic Dynamics, Princeton University Press, Princeton, New Jersey
Byrd, G., Rautiainen, P., Salo, H., et al., 1994, AJ 108, 476
Boer, B., Schulz, H., 1993, A&A 277, 397
Buta, R., Crocker, A.D., 1993, AJ 105, 1344
Colina, L., Pérez-Olea, D., 1992, MNRAS 259, 709
Díaz, A.I., Terlevich, E., Terlevich, R.J., 1989, MNRAS 239, 325 (DTT)
Elmegreen, D.M., Elmegreen, B.G., Chromey, F.R., et al., 1996, AJ 111, 1880
Ferrarese, L., Ford, H.C., 1999, ApJ 515, 583
Filippenko, A.V., Sargent, W.L.W., 1985, ApJS 57, 503
Ford, H.C., Dressel, L., Ferrarese, L., Tsvetanov, Z., 1998, in Galaxy Dynamics, ASP Conference Series, edited by D.R. Merritt, M. Valluri, and J.A. Sellwood
Friedli, D., Martinet, L., 1993, A&A 227, 27
Friedli, D., Wozniak, H., Rieke, M., et al., 1996, A&AS 118, 461
García-Vargas, M.L., Mollá, M., Bressan, A., 1998, A&AS 130, 513
Gonçalves, A.C., Véron-Cetty, M.-P., Véron, P., 1999, A&AS 135, 437
González Delgado, R.M., Pérez, E., Tadhunter, C.N., et al., 1997, ApJS 108, 155
González Delgado, R.M., Pérez, E., 1997, ApJS 108, 199
González Delgado, R.M. Leitherer, C., Heckman, T.M., et al., 1998, ApJ 495, 698
González Delgado, R.M., García-Vargas, M.L., Goldader, J., et al., 1999a, ApJ 513, 707
González Delgado, R.M., Leitherer, C., Heckman, T.M., 1999b, ApJ, in press, (astro-ph/9907116)
Ho, L.C., Filippenko, A.V., Sargent, W.L.W., 1995, ApJS 98, 477
Ho, L.C., Filippenko, A.V., Sargent, W.L.W., 1997a, ApJ 487, 568
Ho, L.C., Filippenko, A.V., Sargent, W.L.W., 1997b, ApJS 112, 315
Ho, L.C., Filippenko, A.V., Sargent, W.L.W., et al., 1997c, ApJS 112, 391
Kenney, J.D.P., Wilson, C.D., Scoville, N.Z., et al., 1992, ApJL 395, 79
Kohno, K., Kawabe, R., Vila-Vilaró, B., 1999, ApJ 511, 157
Maiolino, R., Ruiz, M., Rieke, G.H., Papadopoulos, P., 1997, ApJ, 485, 552
McLeod,K.K., Rieke, G.H. 1995, ApJ 441, 96
Marlowe, A.T., Heckman, T.M., Wyse, R.F.G., et al., 1995, ApJ 438, 563
Márquez, I., Moles, M., 1993, AJ 105, 2090
Márquez, I., Moles, M., 1996, A&A 120, 1
Márquez, I., Moles, M., Masegosa, J., 1996, A&A 310, 401
Márquez, I., Durret, F., González Delgado, R.M., et al., 1999a, A&AS, accepted (astro-ph/9909351)
Márquez, I., Durret, F., et al., 1999b, in preparation
Miller, B.W., Bureau, M., Verolme, E., et al., 1999, astro-ph/9906091
Moles, M., Márquez, I., Pérez, E., 1995, ApJ 438, 604
Mulchaey, J.S., Regan, 1997, ApJ 482, L135astro-ph/9909351
Mulchaey, J.S., Regan, M.W., Kundu, A., 1997, ApJS 110, 299
Mundell, C.G., Pedlar, A., Baum, S.A., et al., 1995, MNRAS 272, 355
Muñoz-Tuñón, C., Vilchez, J.M., Castañeda, H., et al., 1989, ApSS 157, 165
Peletier, R.F., Knapen, J.H., Shlosman, I., et al., 1999, astro-ph/9905076
Piner, B., Stone, J.M., Teuben, P.J., 1995, ApJ 449, 508

Regan, M.W., Mulchaey, J.S., 1999, AJ 117, 2676
Robinson, A., Vila-Vilaró, B., Axon, D.J., et al., 1994, A&A 291, 351
Rozas, M., Beckman, J.E., Knapen, J.H., 1996a, A&A 307, 735
Rozas, M., Beckman, J.E., Knapen, J.H., 1996b, A&A 312, 275
Saikia, D.J., Pedlar, A., Unger, S.W., et al., 1994, MNRAS 270, 46
Shlosman, I., Frank, J., Begelman, M.C., 1989, Nature 338, 45
Veilleux, S., Osterbrock D.E., 1987, ApJS 63, 295
Vila, M.B., Pedlar, A., Davies, R.D., et al., 1990, MNRAS 242, 379
Vila-Vilaró, B., Robinson, A., Pérez, E., et al., 1995, A&A 302, 58
Wilkins, T.N., Axon, D.J., 1991, TWODSPEC, Starlink User Note, No. 16
Wozniak, H., Friedli D., Martinet L., et al., 1995, A&AS 111, 115

Fig. 1. Full frame B' (a) and *Ks* (b) broad band images of NGC 6951. The images show clearly two spiral arms, the bar, dust lanes along the bar and the circumnuclear ring at 5 arcsec from the nucleus. The orientation in all the images is North up and East to the left. The scale is 92 pc arcsec^{-1}. The contour levels are (a) in B′ 24.0 22.5 21.5 20.5 19.5 19.0, (b) in *Ks* 21.0 20.0 19.5 19.0 18.5 18.0 17.5 17.0 16.5 16 15.5 15.0.

Fig. 2. Broad band photometric parameters as a function of the root square of the distance to the nucleus. Surface brigthness (μ): upper pannels; ellipticity (ϵ): middle pannels; and position angle (PA): bottom pannels. The parameters are derived by fitting isophotal profiles to the images: B' (left pannels); I (middle left pannels); J (middle right pannels) and *Ks* (right pannels).

Fig. 3. Full frame colour images. (a) B'-I and (b) *J*-*Ks*. B'-I traces very well the spiral arms and the circumnuclear ring, where recent star formation is taking place. Dust lanes along the bar are also seen as dark features. Grayscales are displayed between B'-I=3.1 and 1.9, and *J*-*Ks*=-1.0 and -2.0.

Fig. 4. colour images of the bar and inner regions of NGC 6951: (a) B'-K' and (b) I-K'. The inner part of the ring is dominated by blue colours, except for the nucleus that appears as a red central knot. Grayscales are displayed between B'-K'=0.06 and 0.16, and I-K'=0.55 and 1.30.

Fig. 5. *J*-*H* colour image of the central 12″×12″. These images were observed by HST+NICMOS. The spatial scale is 0.075 arcsec pixel^{-1}, and the grayscale has been displayed between *J*-*H*=0.55 and 0.31 mag. The circumnuclear ring is mainly delinated as two short spiral arms. In the inner part of the ring, the dust delineates a multi-spiral structure that ends in the nucleus.

Fig. 6. B'-K' colour image of the central 20×20 arcsec. Hα contours (from the data of González Delgado et al. 1997) are also plotted. Note that there is not a perfect correspondence between the blue knots in the B'-K' image and the nebular emission. The three slit positions for the spectroscopy data are also plotted. Grayscale is displayed between B'-K'=0.05 and 0.16.

Fig. 7. Hα/Hβ emission line ratios (dots) measured along the three slit PA. This ratio has been corrected for underlying stellar absorption as explained in the text. The theoretical ratio predicted by the case B recombination is plotted as a horizontal dashed line. The Hα flux along the slit is also shown as a full line.

Fig. 8. Hα (open circles + dashed line) and [N II] (squares + dashed) fluxes and their ratio [N II]/Hα (filled circles + full line) measured along the three slit PA. Note that the large [N II]/Hα ratio in the inner $\pm$2 arcsec is due to a strong increase in the [N II] flux.

Fig. 9. Hβ (filled circles + dashed line) and [O III] (open points + full line) fluxes along PA=138°. The [O III] emission is mainly concentrated in the inner $\pm$2 arcsec, where the Hβ emission is very weak.

Fig. 10. One dimensional spectrum, from 4750 Å to 5150 Å, of the nucleus and of the two regions on either side of the nucleus along PA=48°. Note that these regions have low excitation, consistent with the gas being photoionized by stars.

Fig. 11. Nuclear spectrum (the central 0.72 arcsec) in the Ca II triplet region. The most relevant lines are labelled. Mg I λ8807 is very strong, indicating that the metallicity is solar. Paschen 14 is very weak, thus Pa13 and Pa15 must contribute very little to the Ca II λ8542 and λ8662, respectively.

Fig. 12. Equivalent width of the Ca II λ8542 + λ8662 lines, measured using the line and continuum windows defined by Díaz et al. (1989). The equivalent width is $\geq$ 7 Å in the nucleus and out to the circumnuclear ring, indicating the presence of red supergiant stars in the central 5×5 arcsec of the galaxy.

Fig. 13. Velocity curve (dots) obtained from the pixel to pixel measurements of the Hα flux (full line), derived fitting a gaussian to the profile of the emission line. Curves are plotted for the three slit positions. At PA=138° (photometric major axis of the galaxy) the curve shows the maximum velocity amplitud. At PA=48° the curve shows more structure than expected for the minor axis of the galaxy. The inset within each figure shows the circumnuclear $\pm$8 arcsec expanded; the three insets have the same scales in both distance and velocity axes, respectively.

Fig. 14. FWHM of the emission lines Hα (filled circles) and [N II] (empty squares). The velocity dispersion of the gas is maximum in the inner $\pm$1.2 arcsec, and minimum at the position of the H II regions in the ring. The Hα flux is plotted as a dashed line.

Fig. 15. Velocity curves from the two strongest CaT absorption lines ($\lambda\lambda$8542, 8662), measured by cross-correlation of the galaxy frames with spectra of K giant stars. The velocity curve of the ionized gas (dots) is shown for comparison with the stellar velocity curve (circles). In the central region the CaT absorption lines are resolved in two components, plotted as filled and open circles. The insets show the central $\pm$10 arcsec; the three have the same radial and velocity scales respectively, and the gas velocity has been plotted as a full line. Notice how in the inner $\pm$2 arcsec, the stars and the ionized gas follow the same velocity pattern at PA=84° and 138°, but not along the minor axis, where the Hα curve presents more structure.

Fig. 16. HST WFPC2 *V* (a) and NICMOS *H* (b) images of the circumnuclear region. To show more clearly the morphological structure of the cicumnuclear region, the original images have been sharp enhanced by dividing them by the corresponding median filtered image. Note the spiralling structure delineated by dust in the *V* image down into the nucleus.

Table 1. Journal of observations

telescope - PA (°)	sampling[a]	wavelength (Å)	t_{exp} (s)	airmass
WHT - 138	0.36″	4757–5141	1800	1.32
WHT - 138	0.36″	6493–6881	1800	1.36
WHT - 138	0.36″	8506–8882	3600	1.34
WHT - 84	0.36″	4757–5141	1800	1.27
WHT - 84	0.36″	6493–6881	1800	1.26
WHT - 84	0.36″	8506–8882	3600	1.26
WHT - 38	0.36″	4757–5141	1800	1.27
WHT - 38	0.36″	6493–6881	1800	1.26
WHT - 38	0.36″	8506–8882	3600	1.26
NOT	0.18″	B'	3000	1.36
NOT	0.18″	I	660	1.51
NOT+ARNICA	0.51″	J	1760 (440)	1.25
NOT+ARNICA	0.51″	Ks	3520 (880)	1.5
3.5m CAHA	0.32″	K'	300	1.22
HST - WFPC2	0.046″	V (547M)	300	
HST - NICMOS2	0.075″	J (110W)	128	
HST - NICMOS2	0.075″	H (160W)	128	

[a] Spatial sampling in arcsec per pixel. The linear dispersion is 0.39 Å pixel^{-1} for all the spectroscopic observations.

Table 2. Electron density along the slit

PA	distance (arcsec)	density cm^{-3}
138° SE	-4.5	530
138° SE	-1.1	1440
138° nuc	0.0	1340
138° NW	1.0	990
138° NW	4.5	290

Table 3. High excitation ratio [O III]/Hβ

PA	orientation	extraction arcsec	F(Hβ) 10^{-15} erg s^{-1} cm^{-2}	F(5007)/F(Hβ)	F(5007)/F(Hβ) corrected[a]
138°	SE	-5.69,-2.82	1.13	0.08	0.07
138°	nuc	-1.40, 1.11	0.20	16.26	5.51
138°	NW	2.54, 5.40	1.17	0.03	0.03
84°	E	-4.00,-1.80	0.38	0.36	0.29
84°	nuc	-1.10, 1.40	0.17	24.82	7.03
84°	W	2.70, 4.90	0.52	0.14	0.12
48°	NE	-4.11,-1.61	0.56	0.30	0.25
48°	nuc	-0.89, 1.25	0.37	16.57	7.96
48°	SW	1.97, 4.47	0.23	0.53	0.39

[a] Hβ corrected for an absorption equivalent width of 1 Å in the nucleus and 0.5 Å in the H II regions.

This figure "fig1.jpg" is available in "jpg" format from:

http://arXiv.org/ps/astro-ph/9909495v1

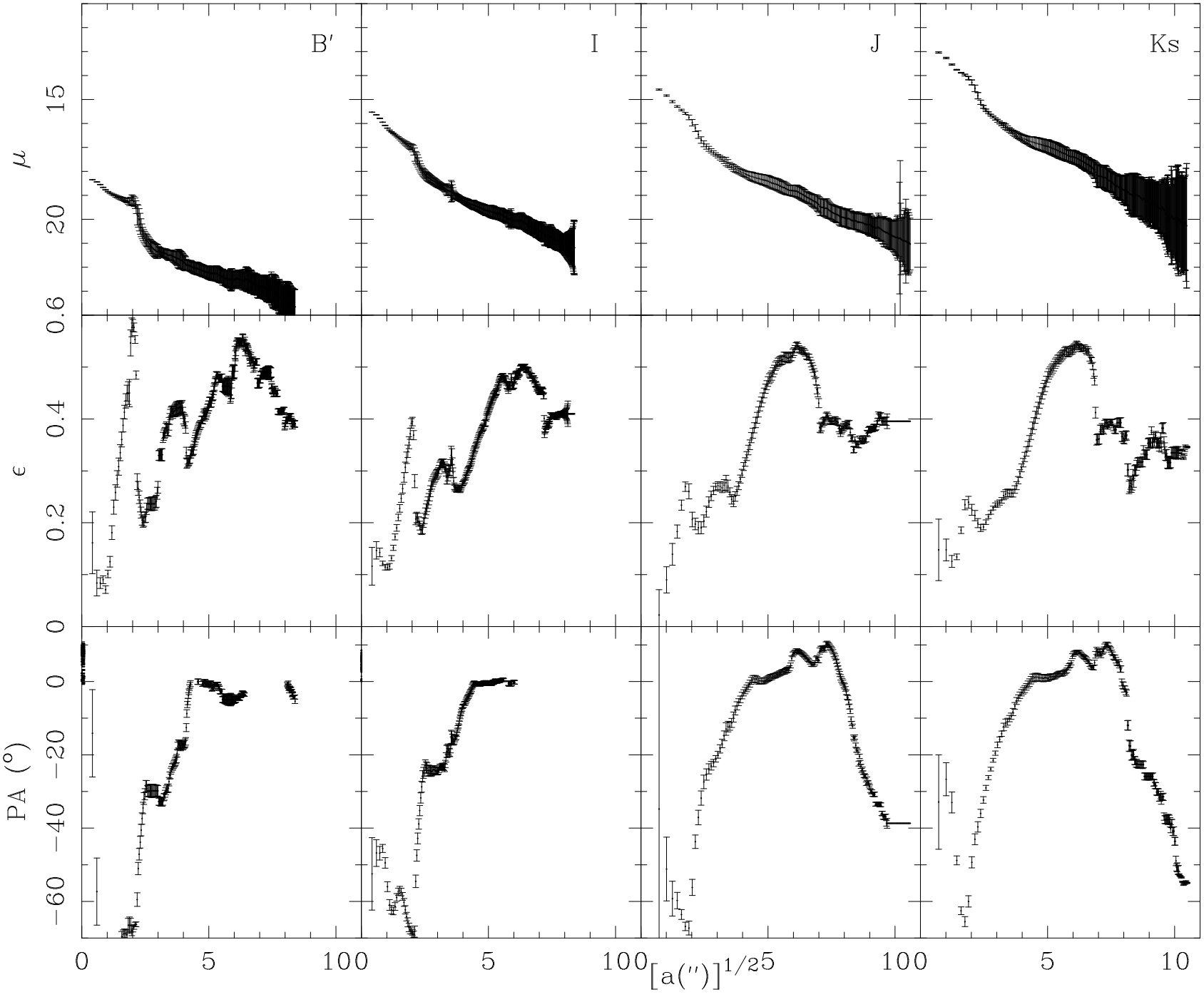
B′
I
J
Ks
μ
ε
PA (°)
[a(″)]^1/25

This figure "fig3.jpg" is available in "jpg" format from:

http://arXiv.org/ps/astro-ph/9909495v1

This figure "fig4.jpg" is available in "jpg" format from:

http://arXiv.org/ps/astro-ph/9909495v1

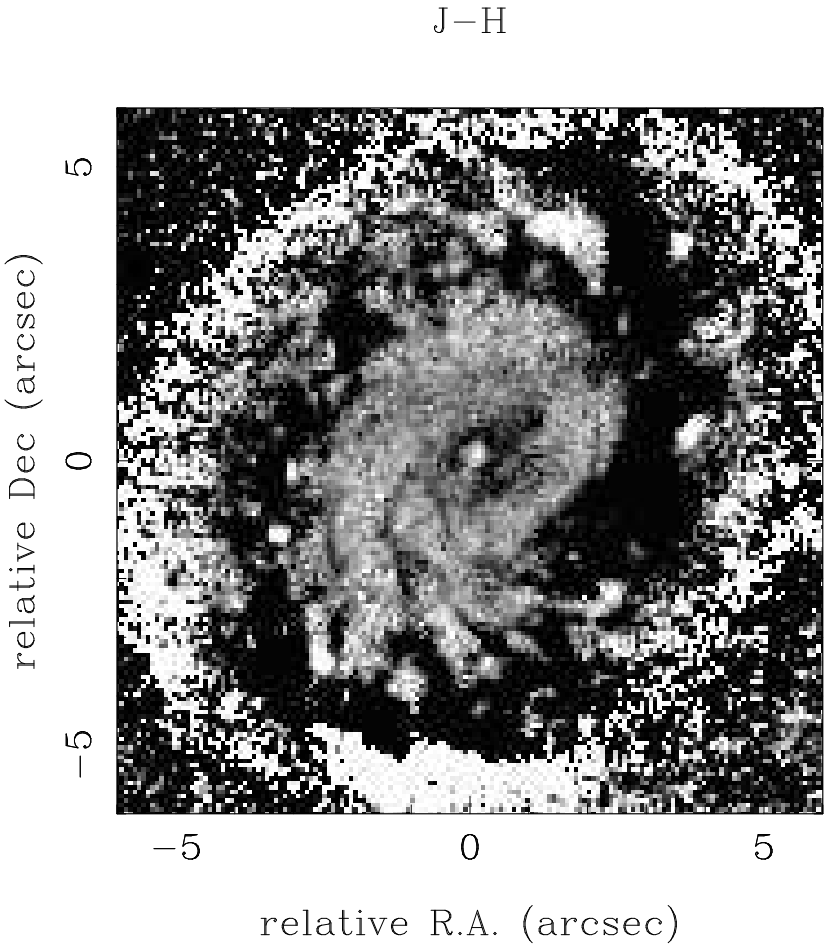
J−H
relative Dec (arcsec)
5
0
−5
−5
0
5
relative R.A. (arcsec)

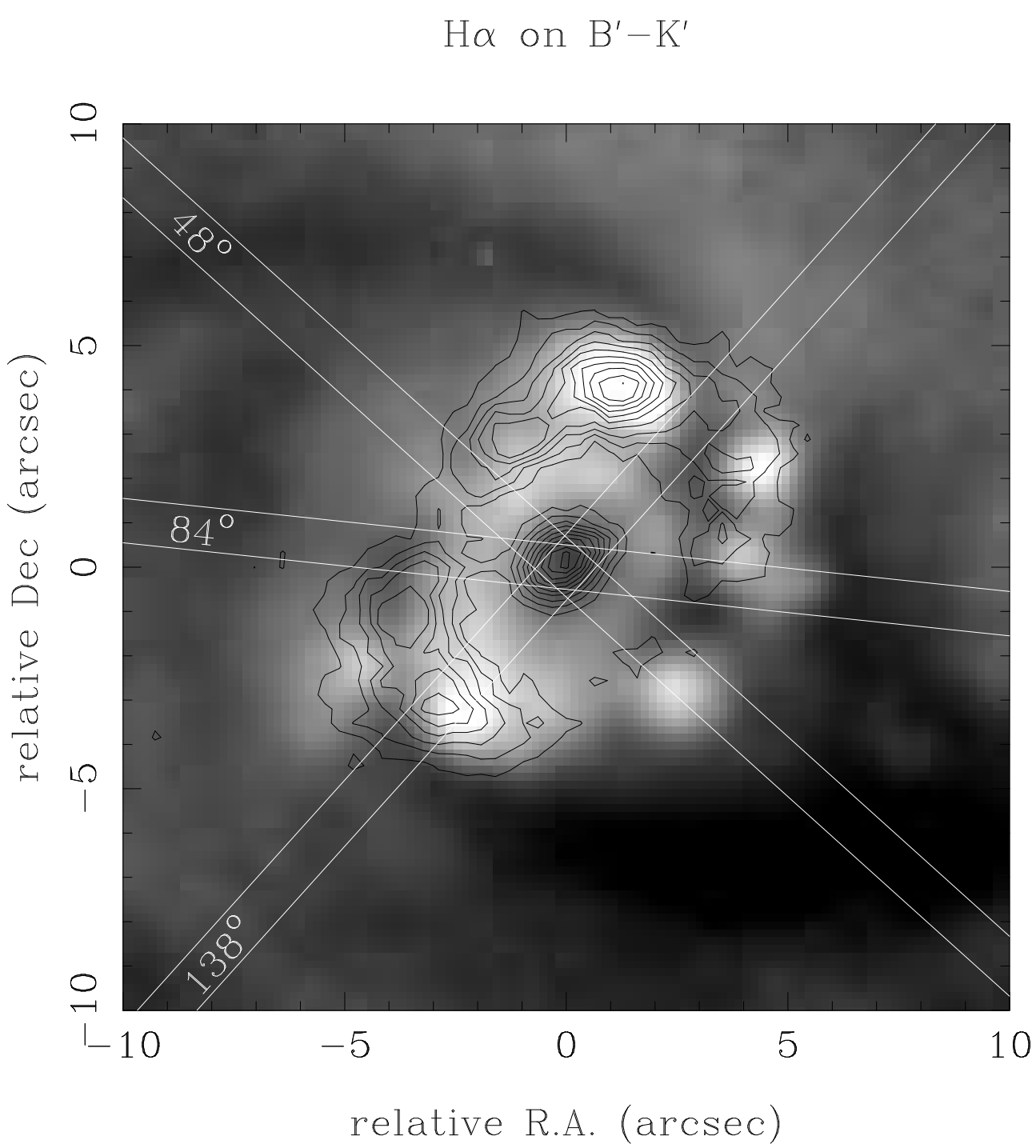
Hα on B′−K′
48°
84°
138°
relative Dec (arcsec)
relative R.A. (arcsec)
10
5
0
−5
−10
−10
−5
0
5
10

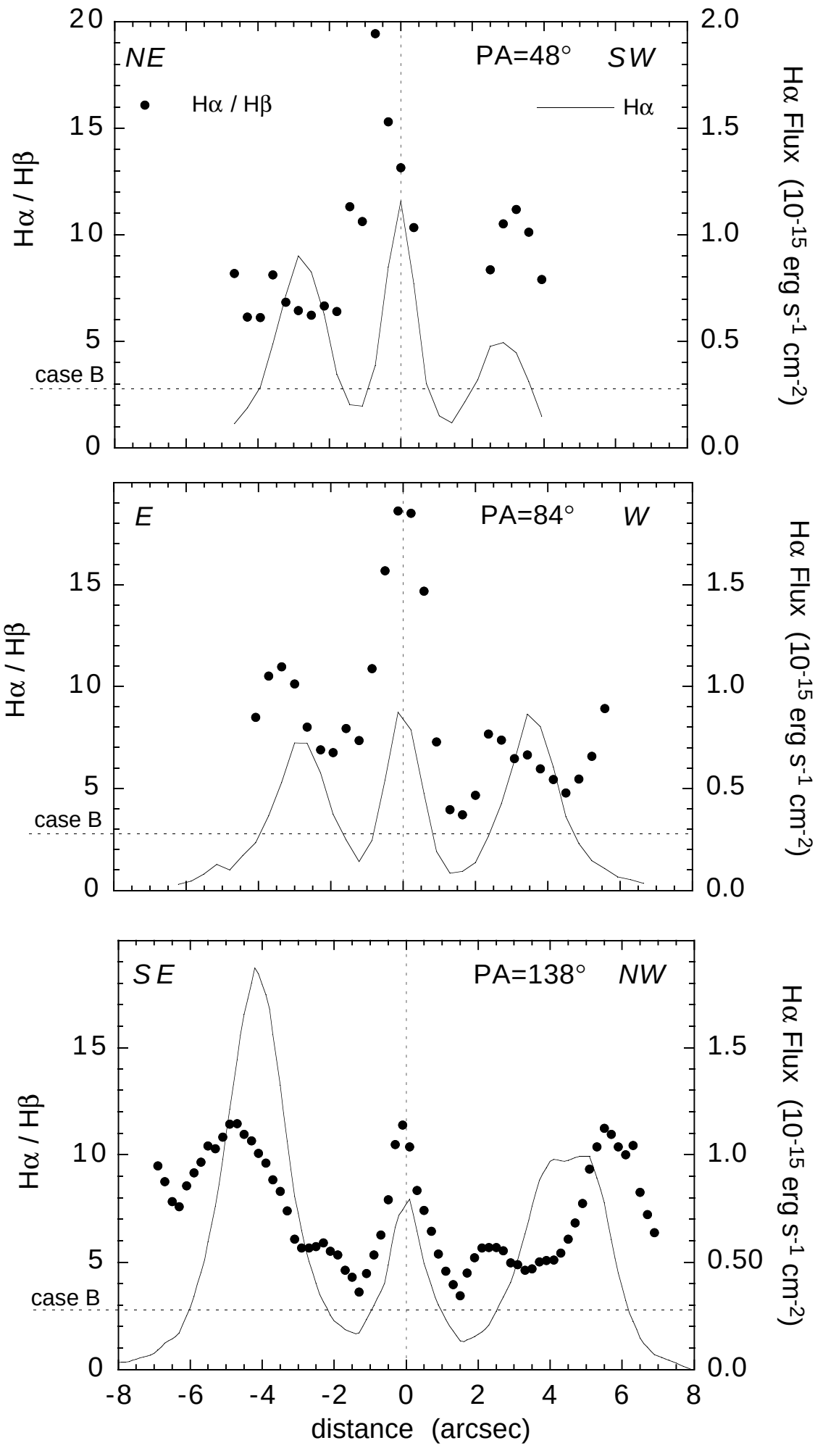
NE
PA=48°
SW
Hα / Hβ
Hα
case B
E
PA=84°
W
case B
SE
PA=138°
NW
case B
Hα / Hβ
Hα Flux (10-15 erg s-1 cm-2)
distance (arcsec)

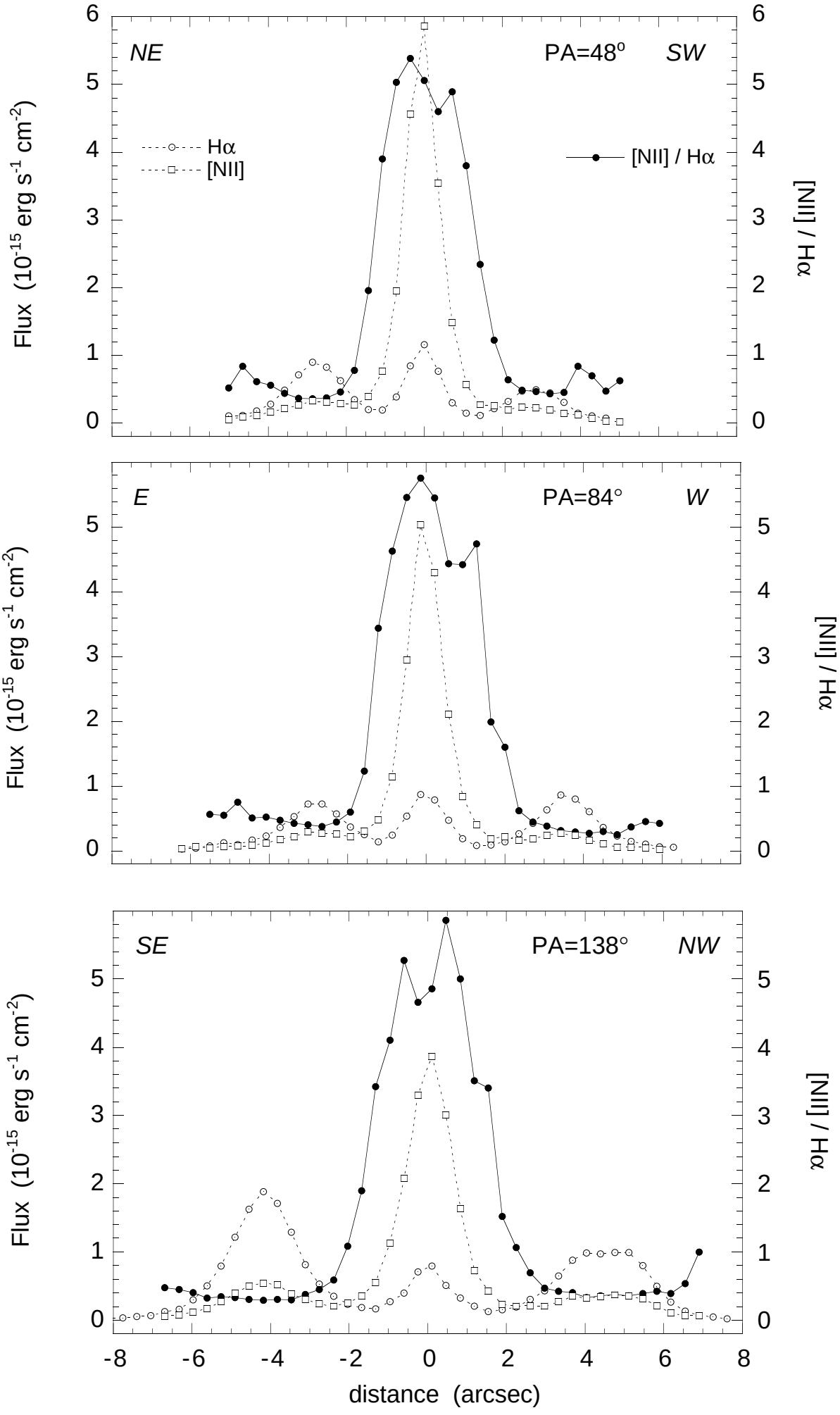
NE
PA=48º
SW
Hα
[NII]
[NII] / Hα
E
PA=84°
W
SE
PA=138°
NW
Flux (10-15 erg s-1 cm-2)
αH / [IIN]
distance (arcsec)

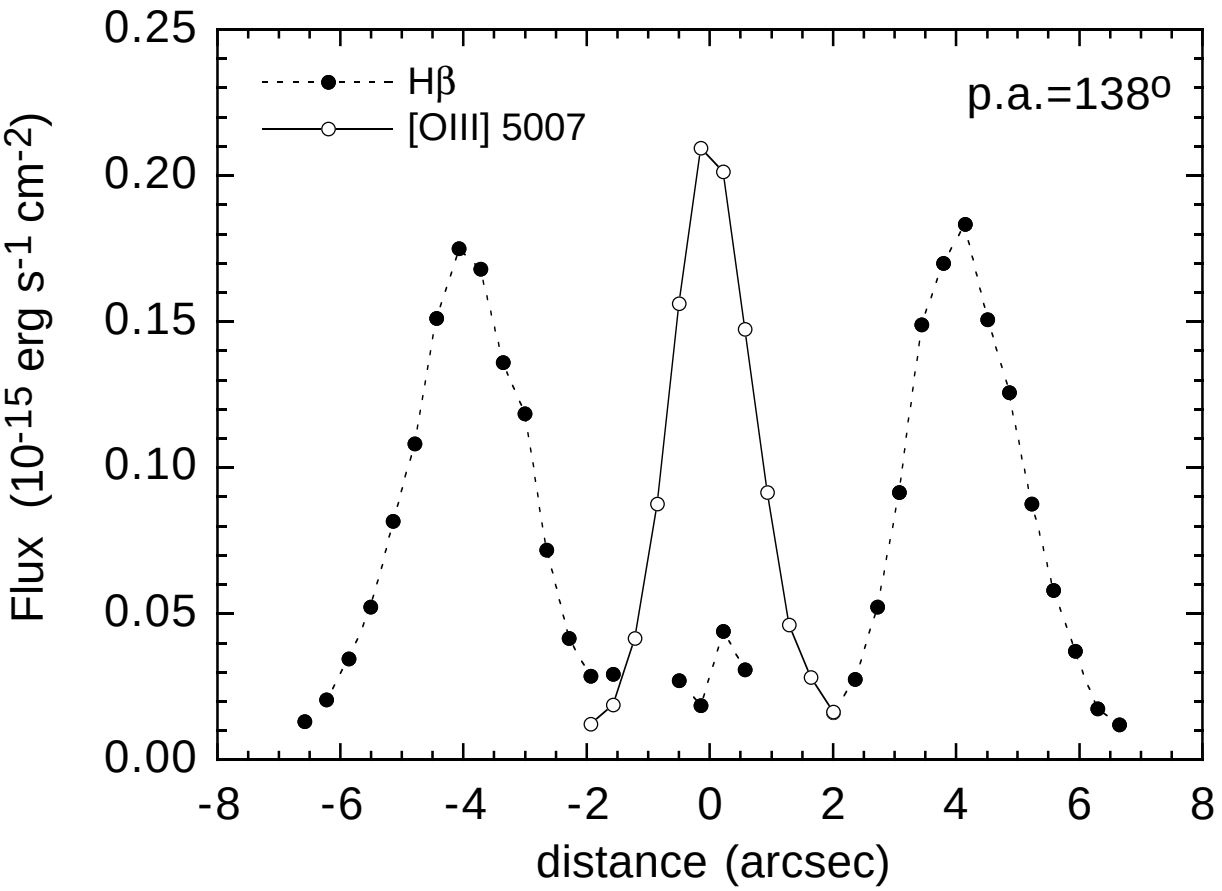
Hβ
[OIII] 5007
p.a.=138º
Flux (10-15 erg s-1 cm-2)
distance (arcsec)
0.25
0.20
0.15
0.10
0.05
0.00
-8
-6
-4
-2
0
2
4
6
8

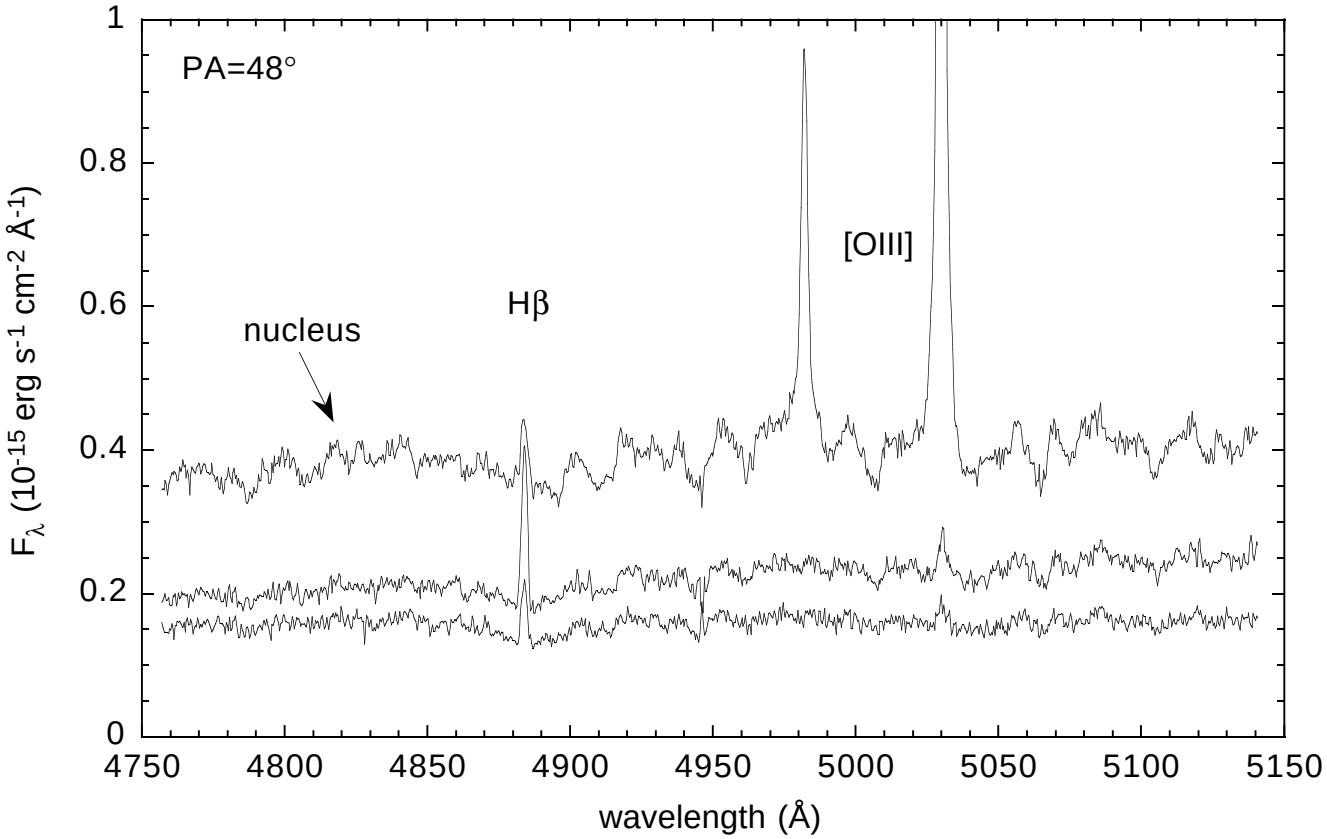
PA=48°
nucleus
Hβ
[OIII]
F_λ (10^{-15} erg s^{-1} cm^{-2} Å^{-1})
wavelength (Å)
0
0.2
0.4
0.6
0.8
1
4750
4800
4850
4900
4950
5000
5050
5100
5150

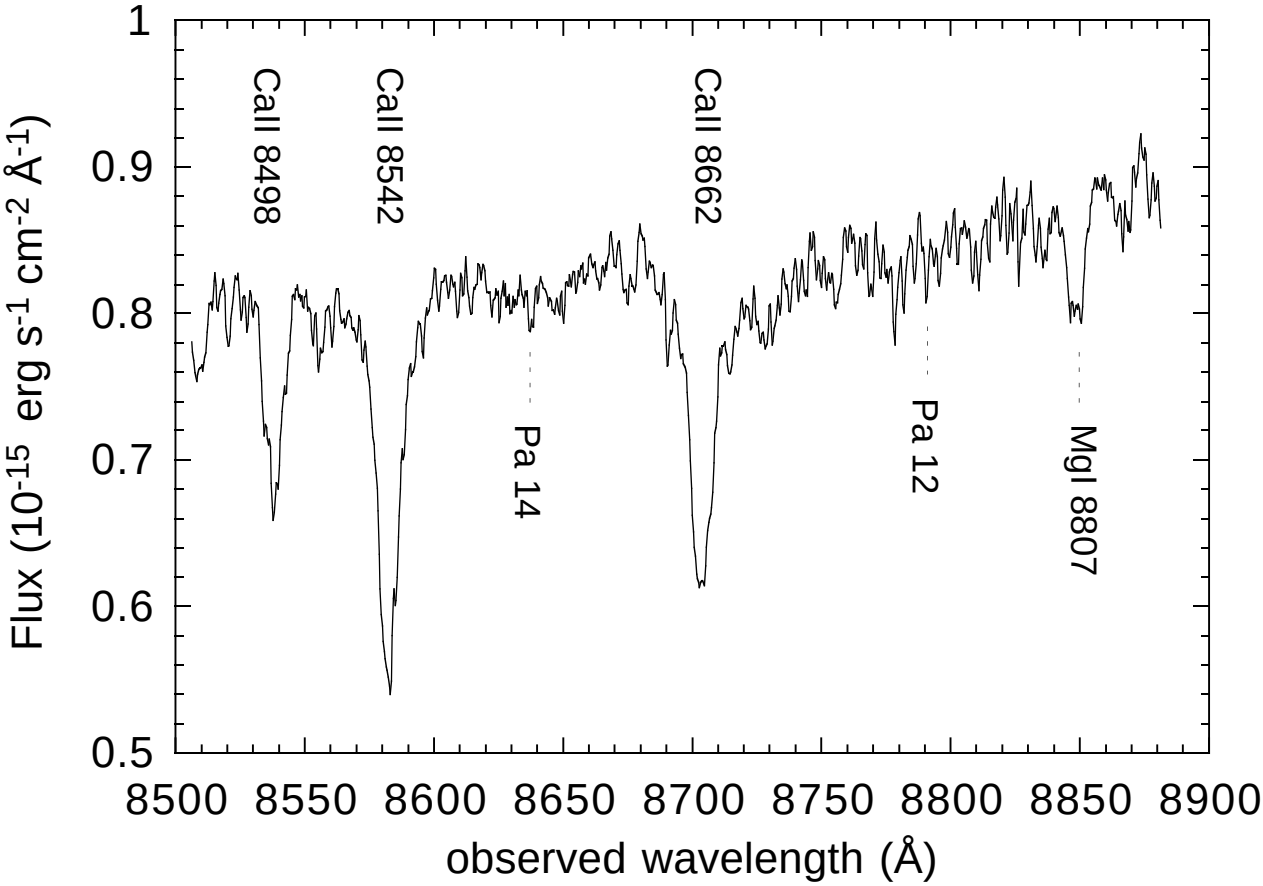
CaII 8498
CaII 8542
Pa 14
CaII 8662
Pa 12
MgI 8807
Flux (10-15 erg s-1 cm-2 Å-1)
observed wavelength (Å)
1
0.9
0.8
0.7
0.6
0.5
8500
8550
8600
8650
8700
8750
8800
8850
8900

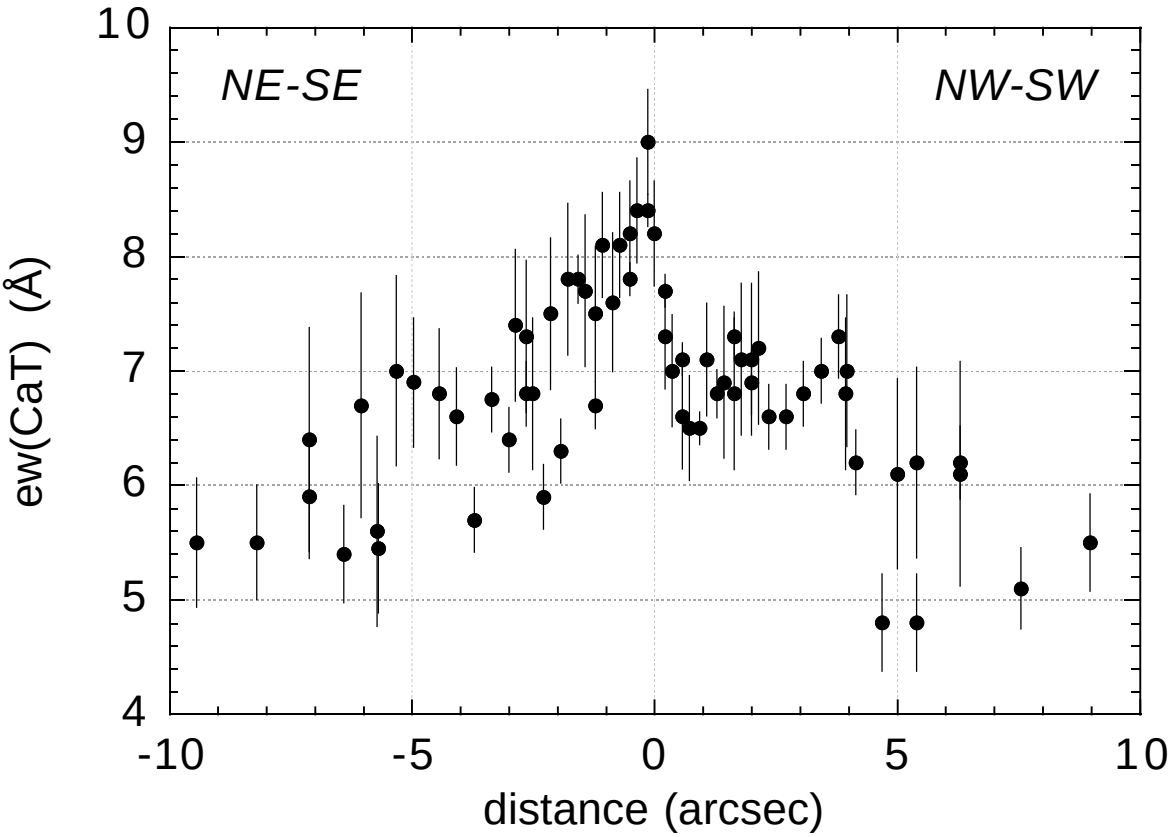
NE-SE
NW-SW
ew(CaT) (Å)
distance (arcsec)
10
9
8
7
6
5
4
-10
-5
0
5
10

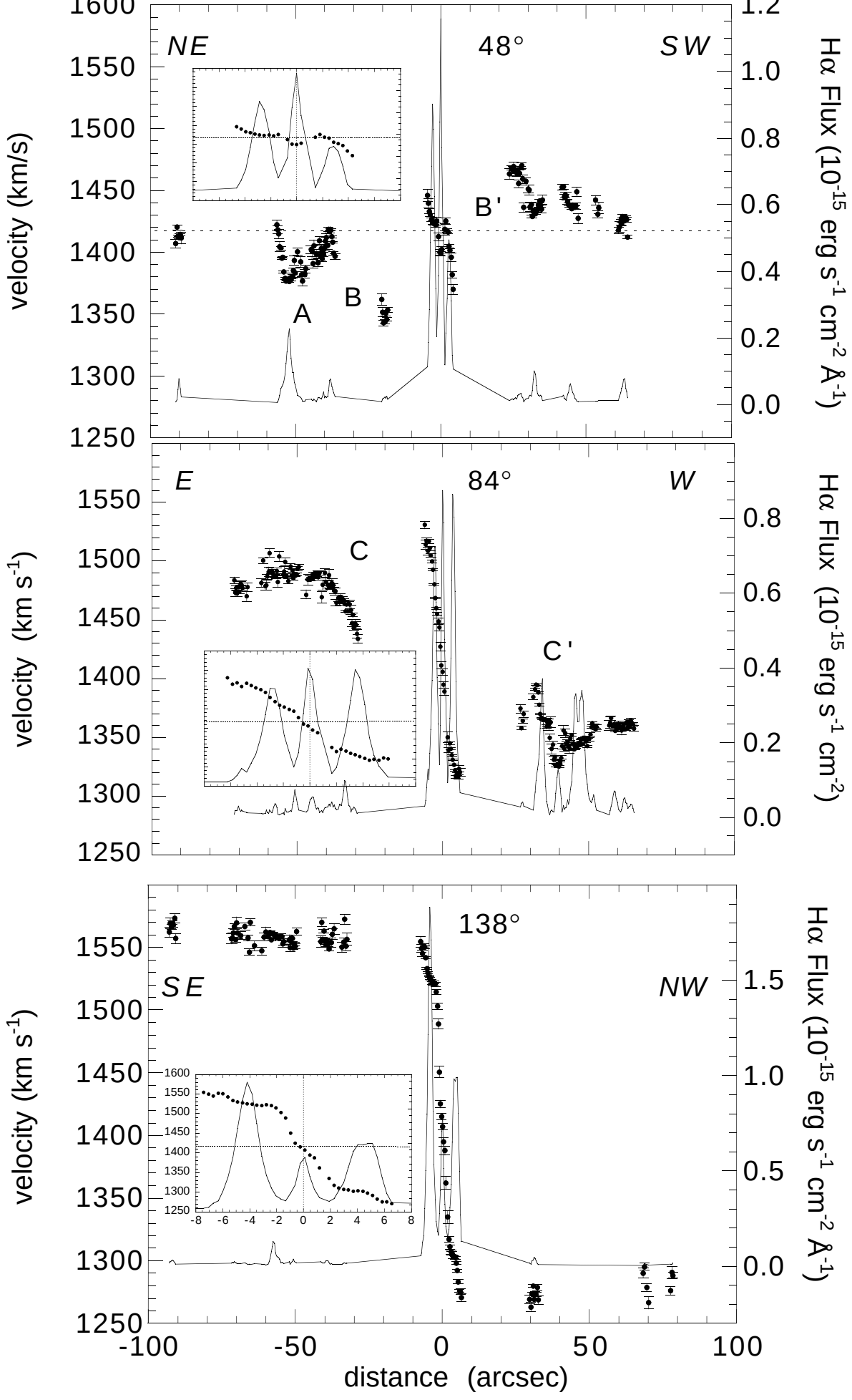
NE
48°
SW
B'
B
A
velocity (km/s)
Hα Flux (10-15 erg s-1 cm-2 Å-1)
E
84°
W
C
C'
velocity (km s-1)
Hα Flux (10-15 erg s-1 cm-2)
SE
138°
NW
velocity (km s-1)
Hα Flux (10-15 erg s-1 cm-2 Å-1)
distance (arcsec)

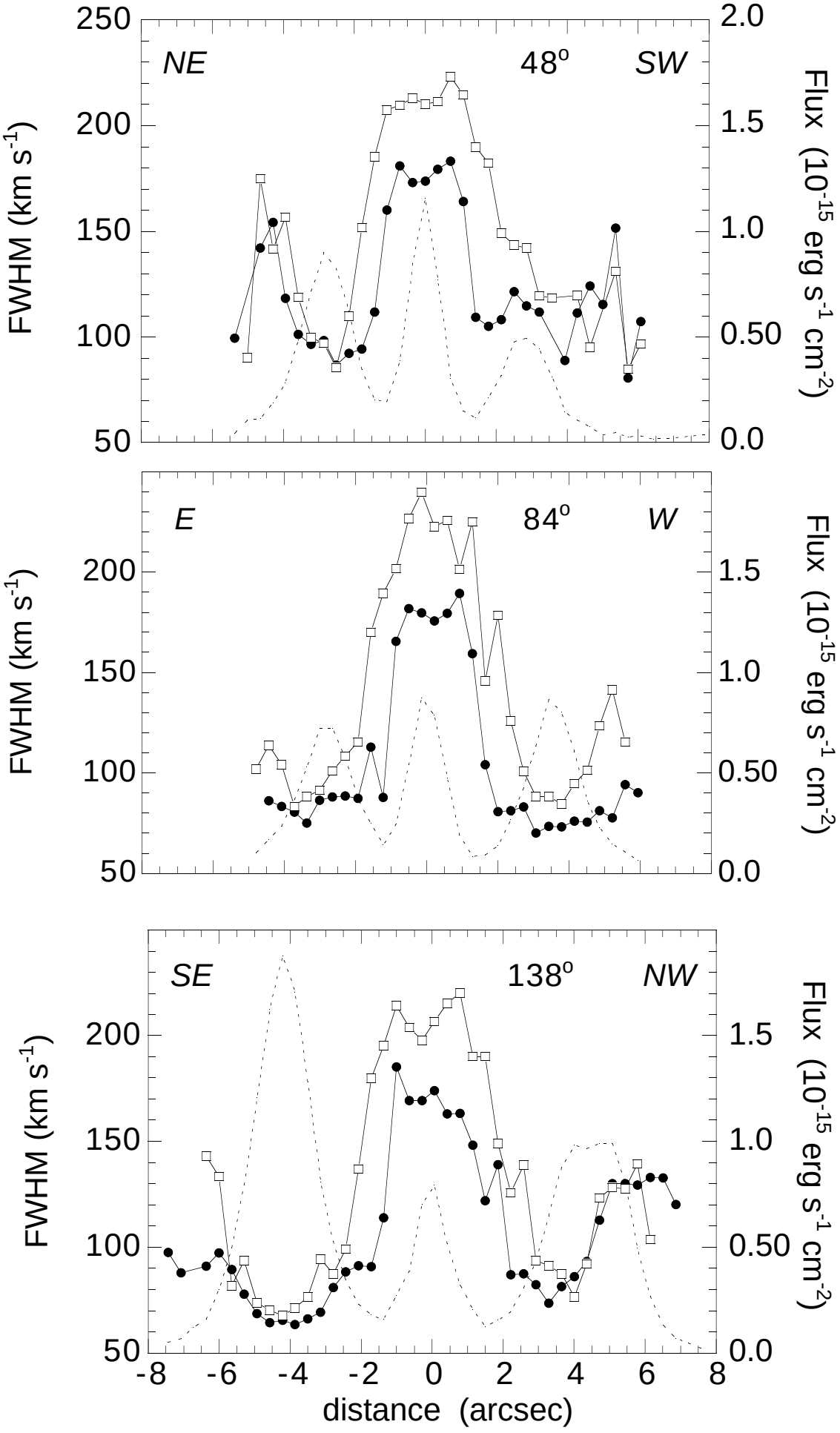
NE
48°
SW
E
84°
W
SE
138°
NW
FWHM (km s-1)
Flux (10-15 erg s-1 cm-2)
distance (arcsec)
250
200
150
100
50
2.0
1.5
1.0
0.50
0.0
-8
-6
-4
-2
0
2
4
6
8

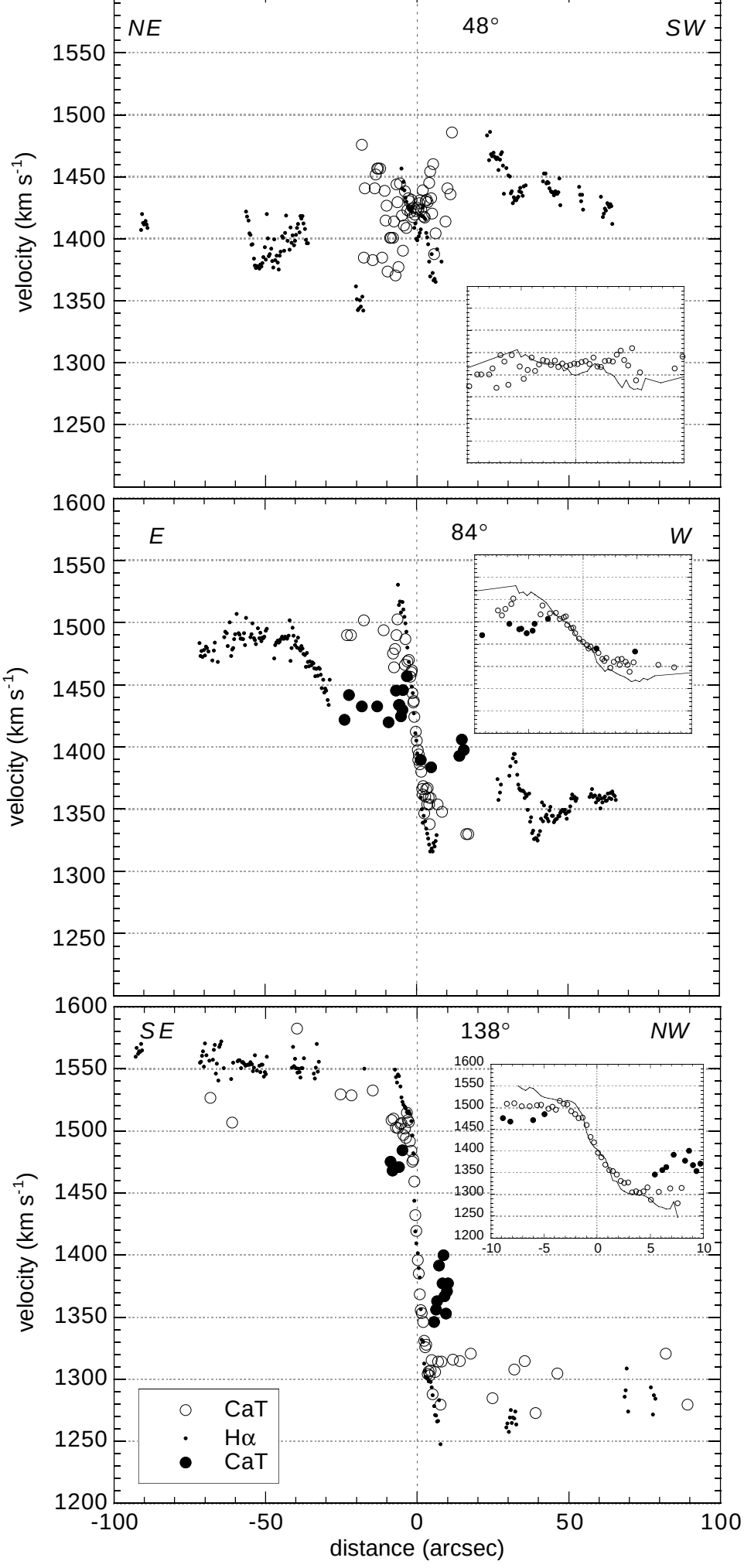
NE
48°
SW
E
84°
W
SE
138°
NW
velocity (km s-1)
distance (arcsec)
CaT
Hα
CaT

V sharp

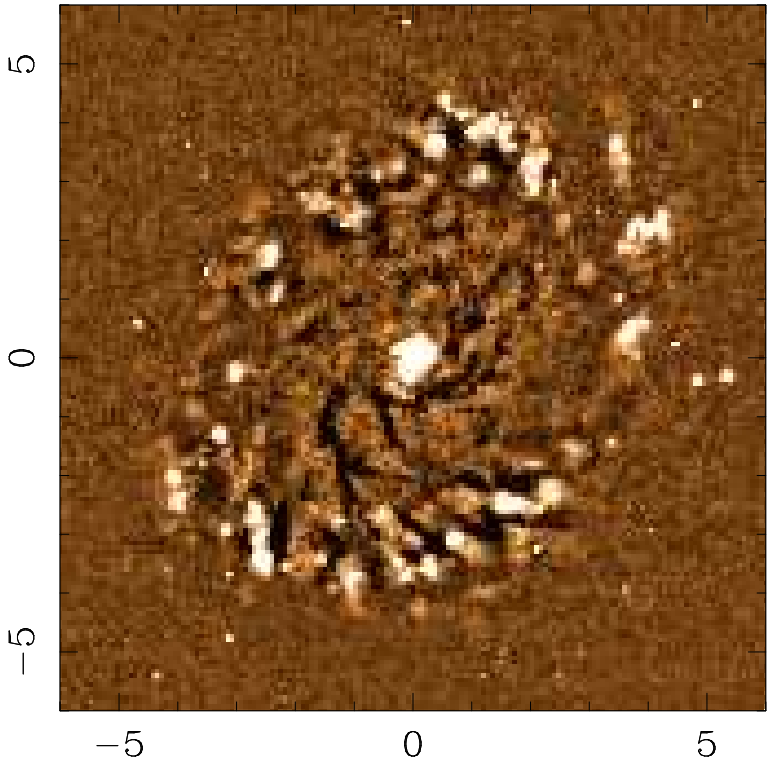
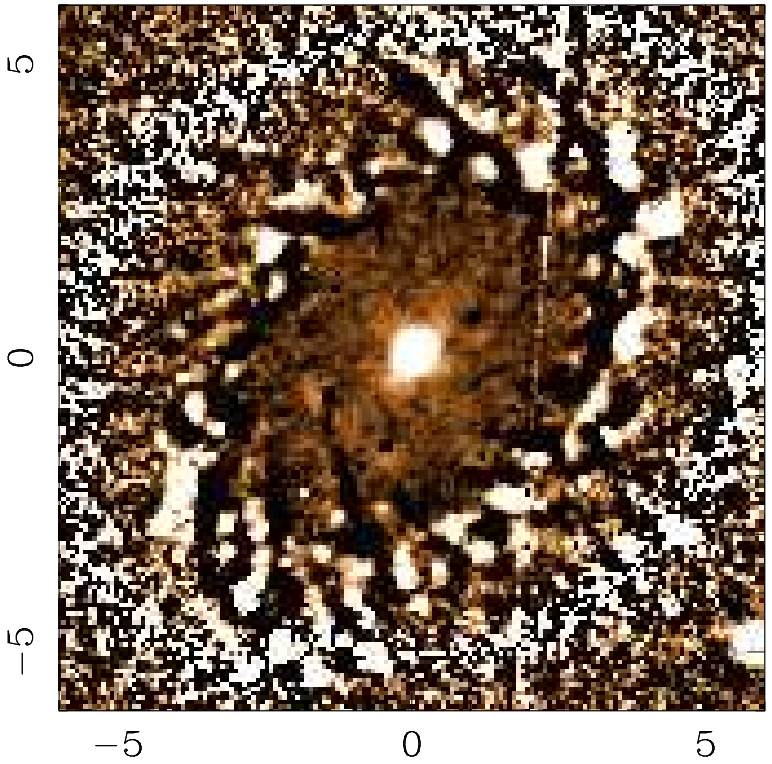
H sharp